

EVALUATION OF USING FERROFLUID AS AN INTERFACE MATERIAL FOR A FIELD-
REVERSIBLE THERMAL CONNECTOR

A Thesis

Presented to

The Faculty of the Graduate School

At the University of Missouri

In Partial Fulfillment

Of the Requirements for the Degree

Masters of Science

By

AHMED S. YOUSIF

Gary L. Solbrekken, Thesis Supervisor

July 2013

The undersigned, appointed by the dean of the Graduate School,

have examined the Thesis entitled

EVALUATION OF USING FERROFLUID AS AN INTERFACE MATERIAL FOR A FIELD-

REVERSIBLE THERMAL CONNECTOR

Presented by Ahmed S. Yousif

A candidate for the degree of

Masters of Science

And hereby certify that, in their opinion, it is worthy of acceptance.

Dr. Gary L. Solbrekken

Dr. Yuwen Zhang

Dr. Stephen Montgomery-Smith

ACKNOWLEDGEMENTS

I would like to gratefully acknowledge the enthusiastic supervision of Dr. Gary Solbrekken who was abundantly helpful and offered invaluable assistance, support, and guidance during this work. Also, deepest gratitude is also due to Dr. Chung-Lung (C.L.) Chen, Dr. Yuwen Zhang and Dr. Stephen Montgomery-Smith; without their knowledge and assistance, this thesis would not have been successful. Special thanks also to all my graduate friends, especially Evan Kontras, Hamid Seyf, John Kennedy, James Armes, Srisharan G. Govindarajan, Philip Makarewicz, Bobby Slater, James Moreleand, and Casey Jesse for invaluable assistance. Finally, yet as importantly, I am forever indebted to my amazing parents and lovely fiancée for their understanding, endless patience and encouragement when it was most required.

TABLE OF CONTENTS

Acknowledgements.....	ii
Table of Contents.....	iii
LIST of FIGURES.....	vi
LIST OF TABLES.....	x
NOMENCLATURE.....	xi
Abstract.....	xiv
Chapter one – Background and objectives.....	1
1.1 What is an Avionics Box?	1
1.2 Wedgelocks.....	4
1.3 Thermal Interface Materials	5
1.2.1 Thermal Paste.....	6
1.2.2 Phase change materials	6
1.2.3 Thermal Tapes	7
1.2.4 Gap Filling Thermal Pads.....	7
1.2.5 Gels.....	7
1.2.6 Adhesives.....	8
1.2.7 The thermal conductivity of the interface material	8
1.4 Thermal Contact Resistance.....	10
1.5 Nanotechnology.....	11
1.6 Nanofluids	12
1.7 Synthesis of Ferrofluids.....	18
1.8 The RevCon Challenge.....	19

1.9 Motivation after RevCon Challenge	21
1.10 Goals to accomplish	22
chapter two– Experimental setup	23
2.1 Introduction	23
2.2 Post RevCon issues and analysis	23
2.3 Installing the Heat Source and Thermocouples	26
2.4 Installing the Magnets.....	27
2.5 Installing the wiping material.....	30
2.6 Cooling Block setup	32
2.7 Thermocouples and Electrical Setup.....	34
Chapter three – experiments and results.....	36
chapter four – Analytic modeling of the system	46
4.1 Ferrofluid design	46
4.2 Wedgelock design	52
chapter five – Numerical analysis	57
5.1 introduction.....	57
5.2 Ferrofluid Design	58
5.2.1 System Modeling and Meshing	58
5.2.2 Results, Mesh Study and Accuracy Check.....	59
5.3 Wedgelock Design	66
5.3.1 System Modeling and Meshing	66
5.3.2 Results, Mesh study and Accuracy Check.....	68
chapter six – Magnetic analysis	74
6.1 Mathematical Analysis	74

6.2 Numerical Analysis	79
6.2.1 Modeling	80
6.2.2 Results and Post Processing	81
chapter seven – Conclusion and closure	86
Appendix-A-Manufacturing process for the new card	88
Bibliography	93

LIST OF FIGURES

Figure 1: Dynon Avionics box in STOL CH 750 Aircraft	1
Figure 2: The back of the same avionics assembly. Notice the fan and heat sink cooling mechanism	2
Figure 3: KAM-500 Chassis, courtesy of Curtiss-Wright Corporation[3]	3
Figure 4: Avionics chassis with cards attached[4]	3
Figure 5: Wedgelock (a) loose mode. (b) Expanded mode.....	4
Figure 6: Wedgelock in action.....	5
Figure 7:Heat transfer through the contact plane between two solid surfaces [19]	10
Figure 8: Oil and Water Based Ferrofluids.....	17
Figure 9: The RevCon Design	20
Figure 10: Thermal Results of RevCon Analysis	24
Figure 11: Copper-rail Card and Aluminum Card.....	25
Figure 12: The final setup for the card	26
Figure 13:(A): Thermocouple Attached to Card Using Solder Paste.....	27
Figure 14: (A): A Single Neodymium Magnet	29
Figure 15: Wiping Assembly.....	30
Figure 16: Card Before and After being Wiped	31
Figure 17: Cooling Block Dimensions.....	32
Figure 18: Cooling Block with copper pipes installed	33
Figure 19: Cooling System Setup	33

Figure 20: Heater Electric Setup	34
Figure 21: The Device with the Ferrofluid Design Card Attached	35
Figure 22: Thermal Resistance Versus Time for Water Based Ferrofluid for aluminum card	37
Figure 23: Thermal Resistance Versus Time for Stability Check (Water Based Ferrofluid)	38
Figure 24: Thermal Resistance Versus Time for Stability Check (Oil Based Ferrofluid) ...	39
Figure 25: Thermal Resistance Versus Time for oil Based Ferrofluid For Aluminum Card	39
Figure 26: Thermal Resistance versus Power (Oil Based Ferrofluid)	40
Figure 27: Card before and after heating	41
Figure 28: Thermal Resistance Versus Time for Stability Check (Wedgelock Design)	42
Figure 29: Thermal Resistance Versus Time for wedgelock design for Aluminum Card ..	42
Figure 30: Thermal Resistance versus Power (Wedgelock Design)	43
Figure 31: Oil Based Ferrofluid Design, water based ferrofluid design and Wedgelock Design.....	44
Figure 32: System to Analyze	46
Figure 33: Equivalent Shape	47
Figure 34: Electrical Equivalent Scheme	48
Figure 35: Card Shape factor details	49
Figure 36: Ferrofluid shape factor Details	49
Figure 37: Shape factor details for Cooling Block	50
Figure 38: Thermal Resistance Versus Clearance	51

Figure 39: Heat transfer Scheme for Wedgelock Design	52
Figure 40: Thermal interfaces between Card, Cooling Block and Wedgelock.....	53
Figure 41: Thermal Conductivity Versus Thermal Resistance	55
Figure 42: Simulation Process	57
Figure 43: Model with Boundary Conditions	59
Figure 44: Scaled Residuals and Number of Iterations.....	60
Figure 45: second Mesh Temperature Distribution for Ferrofluid design.....	61
Figure 46: Second Mesh Heat Flux Distribution for ferrofluid design	62
Figure 47: Mesh Study for ferrofluid design	63
Figure 48: Numerical Relation between Gap Spacing and Thermal Resistance	64
Figure 49: Numerical Relation between Gap Spacing and Thermal Resistance for very small gaps.....	65
Figure 50: Numerical Model for Wedgelock Design	68
Figure 51: Scaled Residuals and Number of Iterations for wedgelock design	69
Figure 52: Temperature Distribution for the Wedgelock Design (First Mesh).....	70
Figure 53: Heat flux Direction	71
Figure 54: Heat flux Distribution.....	71
Figure 55: Mesh Study	72
Figure 56: Thermal Conductivity of wedgelock Versus the Thermal Resistance.....	73
Figure 57: Forces Acting upon Ferrofluid	75
Figure 58: H-Field versus B-Field. Any Value to the right of the vertical line can pull the ferrofluid upward.....	77

Figure 59: H-Field versus the Magnetic Force. Again, the values to the right of the vertical line can pull the ferrofluid upward.	78
Figure 60: B-Field versus Magnetic Force. The values to the right of the vertical line can pull the ferrofluid upward.	78
Figure 61: Finite Elements Method Magnetics (FEMM) Main Screen.....	80
Figure 62: FEMM Model for Ferrofluid Design	81
Figure 63: Relation between Coercive force and magnetic flux density	83
Figure 64: Magnetic Flux Density Distribution	84
Figure 65: Vector representation for the Flux Density, showing its direction	84
Figure 66: B-Field density drop along the height of the card	85
Figure 67: H-Field intensity drop along the height of the card	85
Figure 68: Dimensions for New Card	88
Figure 69: Plain milling cutter tool.....	89
Figure 70: Card After first Horizontal Milling.....	89
Figure 71: Card After Second Horizontal Milling	90
Figure 72: Card After Third Horizontal Milling.....	90
Figure 73: Corner Rounding Tool	91
Figure 74: Final Shape	92

LIST OF TABLES

Table 1: Typical Components of Water Based Ferrofluid	16
Table 2: Typical Components of Oil Based Ferrofluid.....	18
Table 3: The Utilized Boundary Conditions.....	58
Table 4: Mesh Study for ferrofluid design	61
Table 5: Numerical Study for Gap Spacing (ferrofluid design)	63
Table 6: Conductance of the thermal Interfaces for wedgelock design.....	66
Table 7: Boundary Conditions for Wedgelock Design	67
Table 8: Mesh Comparison for wedgelock design	69
Table 9: Results of Mathematical Analysis	77
Table 10: Results of numerical analysis	82

NOMENCLATURE

A	Area, square meters
C	Celsius, proportional constant
B	k_p/k_f
b	Particle radius
D_f	diameter of the base fluid molecule
D_n	diameter of a nanoparticle
h	Henry
h_c	contact conductance
h_g	The gap conductance
h_j	The thermal joint conductance
H_c	Surface Microhardness, Coercivity (CH7)
g	Gravitational acceleration
k	Thermal Conductivity
k_c	Thermal conductivity of contact
k_e	Effective thermal conductivity
k_f	thermal conductivity of base fluid
k_m	Thermal conductivity of the polymer matrix

k_p	Thermal conductivity of particles (fillers)
k_s	harmonic mean thermal conductivity of the interface
K	Temperature, Kelvin
m	The surface asperity slope
m_f	Mass of ferrofluid
M	Gas Parameter
N	Normal force
n	Particle volume fraction
P	The contact pressure
Pr	Prandtl number defined by random motion velocity of nanoparticles and dynamic viscosity of the base fluid
Q	Thermal Power (W)
R_c	Thermal resistance of aluminum card
R_{CB}	Thermal resistance of cooling block
R_{FF}	Thermal resistance of ferrofluid
R_{CB}	Thermal resistance of the cooling block
R_{th}	Thermal Resistance, C/W
Re_{dp}	Reynolds number defined by

random motion velocity of
nanoparticles and dynamic
viscosity of the base fluid

Sec	Time, Seconds
T_{CB}	Temperature of the cooling block
V	Volts
W	Power, Watt
x	distance travelled by heat, meters
α	Biot number
β	$(B - 1)/(B + 2)$
γ	Ratio of the nanolayer thickness to the original particle radius
σ	The effective RMS surface roughness.
Υ	The effective gap thickness
μ	Coefficient of friction
Φ	Volume fraction of particles

ABSTRACT

The electrical functionality of an avionics chassis is limited due to heat dissipation limits. The limits arise due to the fact that components in an avionic computer boxes are packed very compactly, with the components mounted onto plug-in cards, and the harsh environment experienced by the chassis limits how heat can be dissipated from the cards. Convective and radiative heat transfer to the ambient are generally not possible. Therefore it is necessary to have heat transferred from the components conducted to the edge of the plug-in cards. The heat then needs to conduct from the card edge to a cold block that not only holds the card in place, but also removes the generated heat by some heat transfer fluid that is circulated through the cold block. The interface between the plug-in card and the cold block typically has a high thermal resistance since it is necessary for the card to have the capability to be re-workable, meaning that the card can be removed and then returned to the chassis. Reducing the thermal resistance of the interface is the objective of the current study and the topic of this thesis.

The current design uses a pressure interface between the card and cold block. The contact pressure is increased through the addition of a wedgelock, which is a field-reversible mechanical connector. To use a wedgelock, the cold block has channels milled on the surface with widths that are larger than the thickness of the plug-in card and the un-expanded wedgelock. The card edge is placed in the channel and placed against one of the channel walls. A wedgelock is then placed between the card and the

other channel wall. The wedgelock is then expanded by using either a screw or a lever. As the wedgelock expands it fills in the remaining channel gap and bears against the other face of the plug-in card. The majority of heat generated by the components on the plug-in card is forced to conduct from the card into the wall of the cold block, effectively a single sided, dry conduction heat transfer path.

Having started as a student design competition named RevCon Challenge, work was performed to evaluate the use of new field-reversible thermal connectors. The new design proposed by the University of Missouri utilized oil based iron nanoparticles, commonly known as a ferrofluid, as a thermal interface material. By using a liquid type of interface material the channel gap can be reduced to a few micrometers, within machining tolerances, and heat can be dissipated off both sides of the card. The addition of nanoparticles improves the effective thermal conductivity of base fluid. The use of iron nanoparticles allows magnets to be used to hold the fluid in place, so the electronic cards may be easily inserted and removed while keeping the ferrofluid in the cold block channel. The ferrofluid-based design which was investigated has shown lower thermal resistance than the current wedgelock design. These results open the door for further development of electronic cards by using higher heat emitting components without compromising the simplicity of attaching/detaching cards from cooling plates.

CHAPTER ONE – BACKGROUND AND OBJECTIVES

1.1 What is an Avionics Box?

The challenges and threats of recent life have proven that sophisticated and superior military forces are a must. It is well known that air forces are an important division in any military force. Thus, there is a huge interest in developing more powerful and advanced computer systems for air forces, especially for aircrafts.

Aircrafts have different avionics depending on the purpose, size, and abilities anticipated from these aircrafts. Personal and small aircraft use basic avionics cards that are connected to a monitor screen. Figures 1 and 2 show a simple Dynon avionics assembly mounted in STOL CH 750 aircraft, manufactured by Zenith Aircrafts Co. located at Mexico, MO:



Figure 1: Dynon Avionics box in STOL CH 750 Aircraft

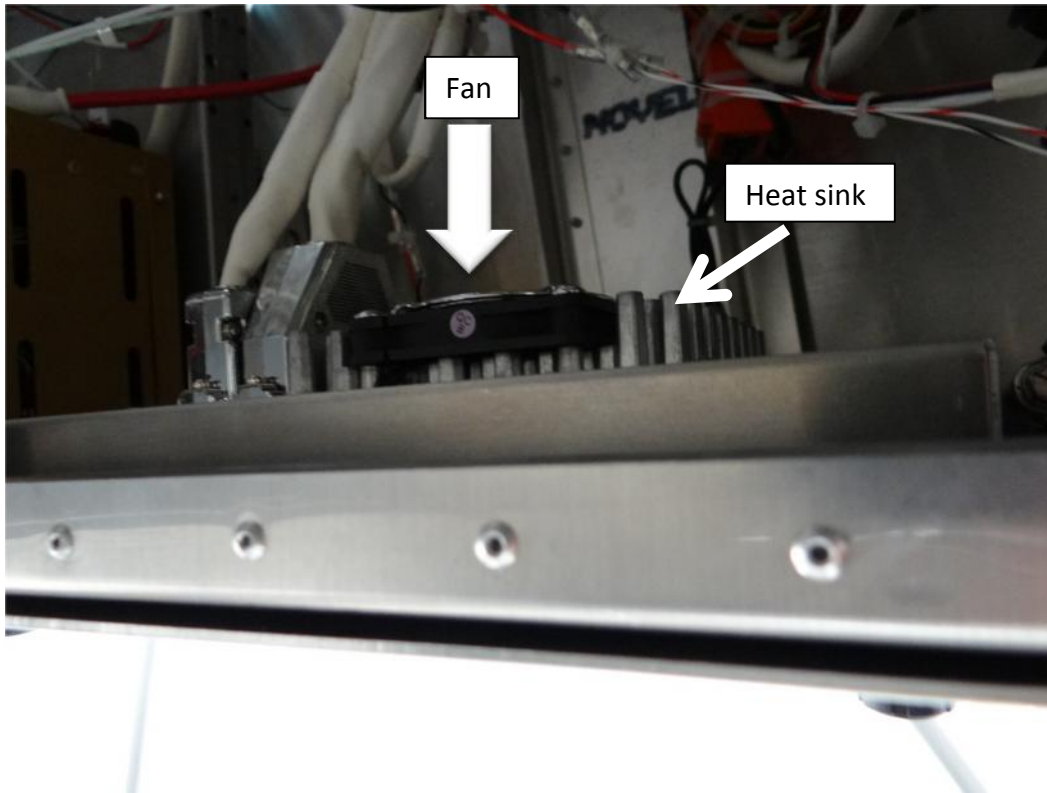


Figure 2: The back of the same avionics assembly. Notice the fan and heat sink cooling mechanism

However, advanced avionics assemblies in high end military aircrafts are much more complicated. They may contain several electronic cards that can be engaged or disengaged from an avionics chassis. The avionics chassis then is connected to the monitoring screen. These cards may enclose RF power amplifiers, which can generate a tremendous amount of heat [1]. Figure 3 and 4 show the KAM-500 avionics chassis manufactured by Curtiss-Wright Corporation. This chassis has been used in two shuttle missions: STS-127 (Endeavour) in July 2009 and STS-133 (Discovery) in February 2011 [2].

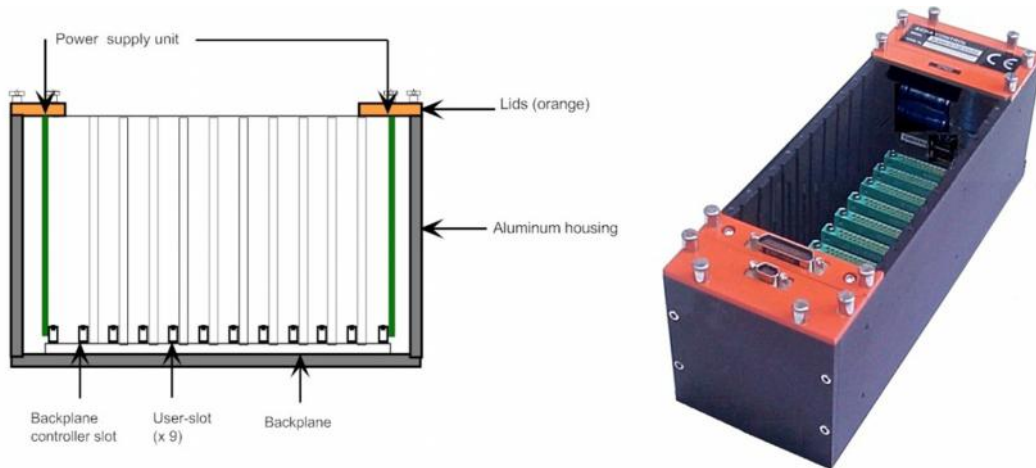


Figure 3: KAM-500 Chassis, courtesy of Curtiss-Wright Corporation[3]

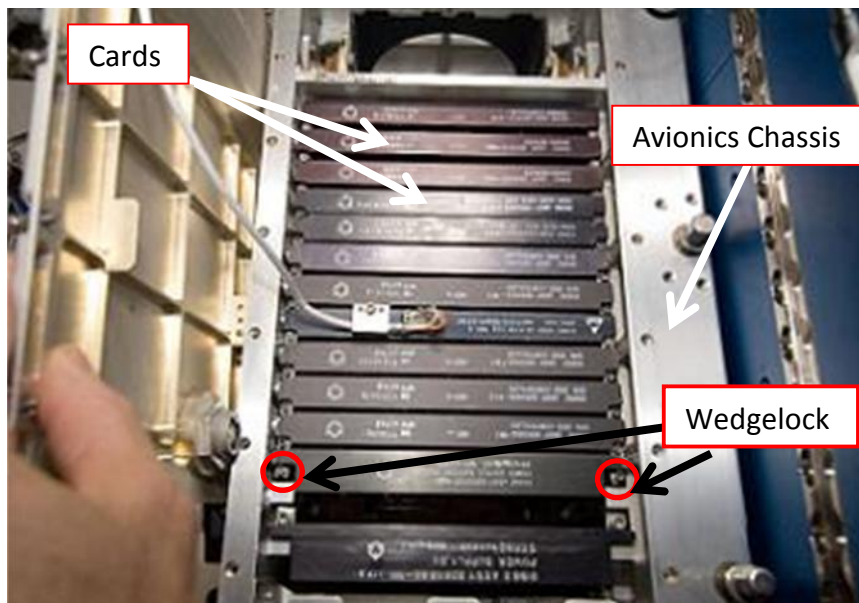


Figure 4: Avionics chassis with cards attached[4]

1.2 Wedgelocks

In avionics systems, one of the most popular methods of mounting electronic cards to an avionics chassis is the use of wedgelocks, which are field reversible thermal connectors. A typical wedgelock consists of a long screw that encloses three or five segments of hollowed aluminum wedges. The screws that are being used in a wedgelock might require a typical screw driver or an Allen wrench, depending on the model of the wedgelock. When the screw is loose, the wedges will align with each other as in figure 5:

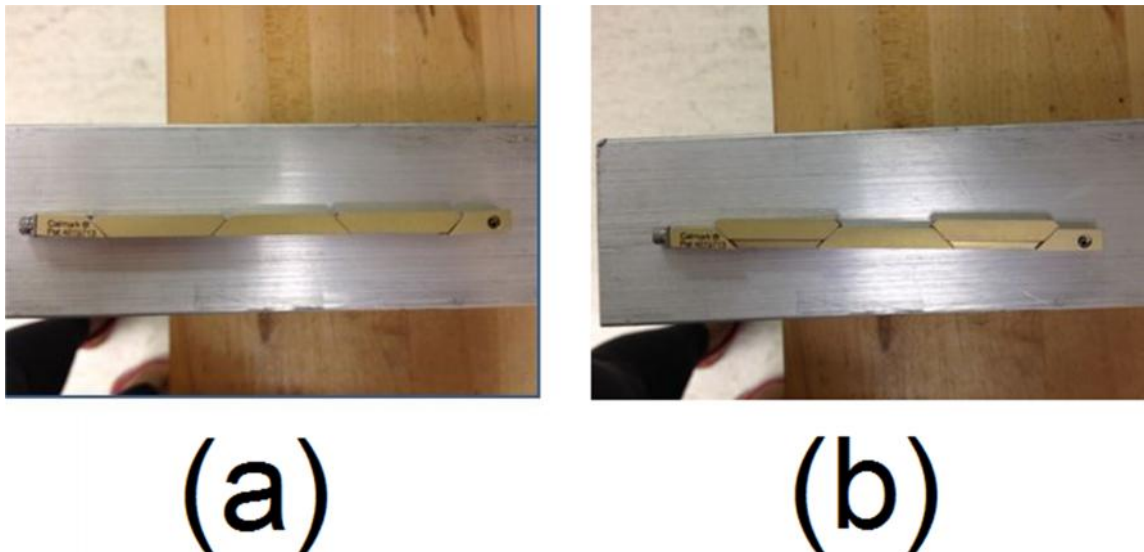


Figure 5: Wedgelock (a) loose mode. (b) Expanded mode

However, when the screw is tightened, the wedgelock segments will slide on each other causing them to move laterally. This movement is necessary to mount cards to a chassis or a cooling block. Figure 6 shows a wedgelock in an expanded mode:

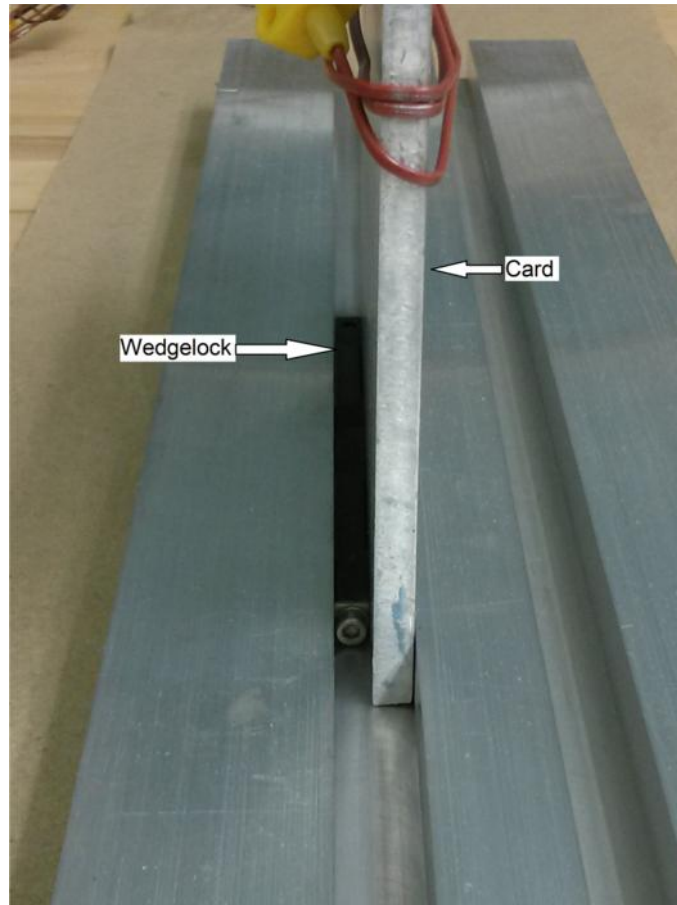


Figure 6: Wedgeloock in action

In addition to what was mentioned above, it is important to note that not all wedgeloocks use screws as a tightening mechanism. Some wedgeloocks use levers instead of screws.

1.3 Thermal Interface Materials

The presence of interstice may decrease the heat transfer rate, and, therefore, the use of thermal interface material could increase the heat transfer rate. There are several kinds of thermal interface materials, such as thermal pastes, phase change, thermal tape, and gap filling thermal pads [5-7].

1.2.1 Thermal Paste

Also called thermal grease, thermal paste is a greasy material that usually consists of a silicon oil matrix loaded with particles, which may be sold in syringes or small containers. Thermal greases usually offer high thermal conductivity, minimum contact pressure, and low viscosity; in addition, they do not require any curing. However, there is possibility of pumping the grease out and phase separation, besides being a chaotic material [8]. The color of the thermal grease could be white to grey depending on its ingredients. Also, thermal conductivity of thermal grease varies according to the application and purpose. For example, Sil-Free™ thermal paste has a self-reported thermal conductivity of 0.79 W/(m.°C)[9], while EVGA's Frostbite has a self-reported thermal conductivity of 6.5 W/(m.°C)[10].

1.2.2 Phase change materials

Phase change materials, sometimes called thermal pads, are materials that have the ability to change their physical conditions at a certain temperature. Such materials might be solid and easy to handle and apply at room temperature since no cure is required. These materials have higher viscosity and increased stability, which leads to less possibility for failure or pumping out. However, they could become soft when pressure and higher temperatures are applied, which results in lower thermal conductivity than greases. Also, these materials require attach pressure in order to be thermal effective, and, thus, a mechanical force is required [6]. As a result, such material can fill most of the interstice between contact surfaces [11]. Polyolefin, epoxy

low molecular weight polyesters and acrylics with BN or Al_2O_3 are good examples of phase change materials [8].

1.2.3 Thermal Tapes

Thermal tapes are conductive and adhesive tapes that require only pressure to perform as interface material. These thermal tapes are soft and can provide wet contact to many surfaces, which means better heat transfer. A thermal tape may contain a ceramic filler and have a dual liner of silicone treated polyester[12].

1.2.4 Gap Filling Thermal Pads

Also known as thermal pads, these pads are foam based thermally conductive and cured silicone gel. These pads are soft and easy to handle since they do not contain any greasy material. Besides, thermal pads do not require special curing or heating before application. Also, they function as shock and vibration absorbers [13].

1.2.5 Gels

Gels are usually made out of Al, Al_2O_3 Ag particles in a silicone or olefin matrices that require curing. In spite of their ability to fit in any interface shape without pumping out, a curing process is needed, which is a disadvantage. Also, gels have relatively low thermal conductivity compared to greases and lower adhesion, which may result in delamination [6].

1.2.6 Adhesives

Adhesives are basically silver particles in a cured epoxy matrix. These materials are able to take the shape of the surface before curing without pumping out or spilling; however, a curing process is needed, which causes high post cure modulus. In addition, there might be a mismatch between the coefficients of thermal expansions that produces stresses [8].

1.2.7 The thermal conductivity of the interface material

There are many models available to find the thermal conductivity of the interface material based on the size and shape of the particles that are being used in these interface materials. Below are some of these models:

- 1- Bruggeman Symmetric Model (BSM) [14]: This model is used for high partial volume fraction to estimate the electrical conductivities of composites [14]. However, this model is not very accurate since it excludes interface resistance between the particles and the matrix (R_b) [14]. The model is shown in equation 1:

$$(1 - \phi) \frac{k_m - k_c}{k_m + 2k_c} + \phi \frac{k_p - k_c}{k_p + 2k_c} = 0$$

(R_b not included)

.....(1)

Φ is the volume fraction of particles in the thermal interface materials.

2- Bruggeman Asymmetric Model (BAM) [14]: This model was modified by Every et al. [15] to include the thermal resistance of the particle-matrix interface. Usually this model is being used for estimating the thermal conductivity of spherical particles of large volume fractions [14]. The model is shown in equation 2 below:

$$(1 - \phi)^3 = \left(\frac{k_m}{k_c} \right)^{(1+2\alpha)/(1-\alpha)} \times \left\{ \frac{k_c - k_p(1-\alpha)}{k_m - k_p(1-\alpha)} \right\}^{3/(1-\alpha)}$$

$$\frac{k_c}{k_m} = \frac{1}{(1 - \phi)^{3(1-\alpha)/(1+2\alpha)}} \text{ for } k_p \gg k_m$$

.....(2)

3- Maxwell-Garnett Model (MG) [14]: This model was proposed for low volume fraction (less than 40%). Since most of thermal interface materials are loaded with more than 60% conductive particles, this model has limited uses [14].

$$\frac{k_c}{k_m} = \frac{[k_p(1+2\alpha) + 2k_m] + 2\phi[k_p(1-\alpha) - k_m]}{[k_p(1+2\alpha) + 2k_m] - \phi[k_p(1-\alpha) - k_m]}$$

$$\alpha = \frac{2R_b k_m}{d}$$

$$\frac{k_c}{k_m} = \frac{(1+2\alpha) + 2\phi(1-\alpha)}{(1+2\alpha) - \phi(1-\alpha)} \text{ for } k_p \gg k_m$$

.....(3)

4- The Percolation Model: The percolation model was proposed to be used for thermal interface materials[16] due to the large difference of conductivities between the particles and the matrix. This model is ideal for cubic particles.

The model is:

$$k_c = k_p (\phi - \phi_p)^2 \text{ valid only for } k_p \gg k_m$$

.....(4)

Where Φ is the volume fraction and Φ_p is the percolation threshold.

1.4 Thermal Contact Resistance

One of the interesting fields in the science of heat transfer is thermal contact resistance. Thermal contact resistance arises as an issue in any conduction problem that involves interaction of two surfaces in contact. Although these surfaces might seem to be in perfect contact; microscopic study for these surfaces shows a lot of imperfections [17, 18], which can affect the heat transfer through conduction:

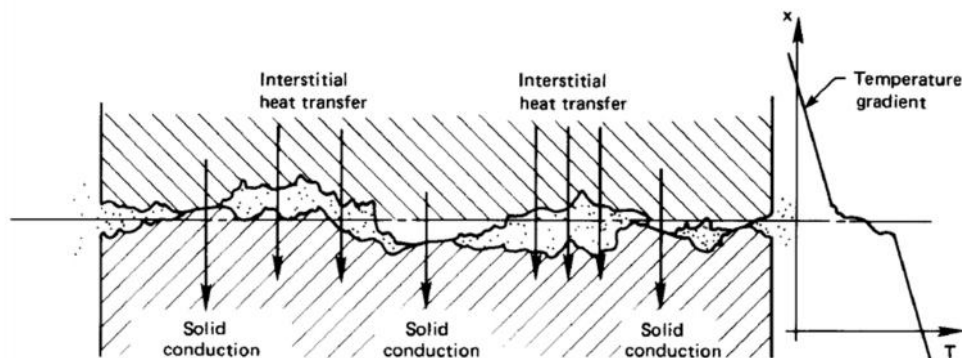


Figure 7:Heat transfer through the contact plane between two solid surfaces [19]

Thus, there is an additional resistance at the contact surfaces caused by the interstitial material. If the interstitial material is air, the case is called dry contact, and it has a relative low thermal conductivity since the thermal conductivity of air is 0.0257 W/m.K; otherwise, if the interstitial material is a liquid, it is denoted as wet contact.

The use of wet contact may reduce the contact resistance and offer better heat transfer if the interstitial material has high thermal conductivity. As a result, thermal interface materials must be investigated.

Yovanovitch[20] provided a correlation to calculate the thermal contact conductance, which is the inverse of the resistance:

$$h_j = h_c + h_g$$

Where h_j is the junction conductance, h_c is the contact conductance, and h_g is the gap conductance. The method is explained in detail in chapter four.

1.5 Nanotechnology

Nanotechnology is one of the fast growing sciences these days. Although the use of the term (Nanotechnology) is fairly new, the science itself has been around for a while. One of the early workers in this field was the famous scientist Einstein, who calculated the size of a single sugar molecule after analyzing the data from the diffusion of sugar in water. Each molecule measured about one nanometer in diameter [21]. After that, in December 1959, Richard P. Feynman presented his famous talk *Plenty of Room at the Bottom* [22]. In his speech, he was focusing on how much space is

available if we go in smaller scales. He presented some examples of his idea, such as writing the Encyclopedia Britannica on the tip of a pin. Besides, Feynman also focused on the importance of improving electron microscopes and how this will advance all sciences rapidly [22]. In 1974, the Japanese scientist Norio Taniguchi defined the term, “nanotechnology” for the first time in a conference [23]. Afterwards, specifically in the year 1977, the American engineer Kim Drexle, while being an undergraduate student at Massachusetts Institute of Technology (MIT), came up with the idea of minuscule robots and how to manufacture any metal from scratch. He published outstanding works in this field. In 1986, he published his famous book *Engines of Creation: The Coming Era of Nanotechnology* [24]. Thus, Drexle inspired many scientists and researchers, and he is considered the “Godfather of Nanotechnology” [25, 26]. Last but not least, it is important to mention the vast effect of the development of the electron microscope on the development of the science of nanotechnology, such as the development of scanning tunneling microscopes in 1981 [27, 28].

1.6 Nanofluids

Nanofluids are systems consisting of dispersed nanoparticles suspended in a fluid base. However, this system is considered as a three phase system because it includes the solid phase, which is the nanoparticles, the liquid phase, which is the fluid base, and the interfacial phase. The interface is very important to the system properties because of their “extremely high surface-to-volume ratio in Nanofluids” [29]. The fluid base material could be water (H₂O), oil, or ethylene glycol (EG) [30].

Classical fluids, such as water and oil, had been used for long time as heat transfer fluids. However, there is a demand to find alternatives due to the fact that classical heat transfer fluids have limited low thermal conductivity [31]. Since metals have relatively high thermal conductivities compared to liquids [32], Researchers suggest that adding nanoparticles to base fluid will considerably increase its static thermal conductivity [31, 33-37]. Moreover, nano-sized particles demonstrate outstanding properties compared to micrometer-sized particles or millimeter-sized particles when it comes to heat transfer since the heat transfer happens on the surface of the particle and since nanoparticles have a large total surface area [31]. Thus, ferrofluids with nanoscale particles are a special case of nanofluids that have an excellent potential as heat transfer fluids. Besides, some researchers found that applying a magnetic field to ferrofluids can enhance the fluid's thermal conductivity, which shows that ferrofluids are suitable for cooling applications under a magnetic field [38]. Moreover, ferrofluids allow for more contact area where nanoparticles can fill most of the gaps, and at the same time the fluid can be maintained in place using magnets. Thus, there is no spilling. The thermal conductivity of ferrofluids may be measured using the method of Transient Hot-Wire, which was proposed by Nagasaka and Nagashima [39] and implemented for nanofluids by Lee and Choi [31] whereas Xue [40] summarized the mathematical models that can be used to find the effective thermal conductivity relative to the base fluid thermal conductivity as follows:

1- Maxwell's Model[41]:

$$\frac{k_e}{k_f} = 1 + \frac{3(B - 1)\phi}{(B + 2) - (B - 1)\phi}$$

.....(5)

B represents the ratio of the thermal conductivity of particles to the thermal conductivity of base fluid. This model was introduced by James Clerk Maxwell and can be used for spherical particles. This model is accurate for a particle volume fraction less than one.

2- Hamilton-Crosser Model[42]:

$$\frac{k_e}{k_f} = \frac{B + (n - 1) - (n - 1)(1 - B)\phi}{B + (n - 1) + (1 - B)\phi}$$

.....(6)

This model was proposed by both Hamilton and Crosser in 1962. The model can be applied to both spherical and non-spherical particles. Again, this model is valid for very small values of the particles volume fraction (much less than one).

3- Jeffery Model[43] :

$$\frac{k_e}{k_f} = 1 + 3\beta\phi + \left(3\beta^2 + \frac{3\beta^3}{4} + \frac{9\beta^3}{16} + \frac{B + 2}{2B + 3} + \frac{3\beta^4}{2^6} + \dots \right) \phi^2$$

.....(7)

The Jeffery model was proposed by David Jeffery in 1973. It is applicable to spherical particles of a high volume fraction and randomly distributed particles.

4- Davis Model [44]:

$$\frac{k_e}{k_f} = 1 + \frac{3(B-1)}{(B+2) - (B-1)\phi} (\phi + f(B)\phi^2 + o(\phi^3))$$

.....(8)

The model was presented by Davis in 1986. This model is valid for high particle volume fraction.

5- Lu-Lin Model [45]:

$$\frac{k_e}{k_f} = 1 + B\phi + b\phi^2$$

.....(9)

This model was introduced by Shih-Yuan Lu in 1996. This model works for both spherical and non-spherical particles. Also, near and far field pair interactions are considered.

6- Yu and Choi [46]:

$$\frac{k_e}{k_f} = \frac{k_p + 2k_f + 2(k_p - k_f)(1 + \gamma)^3\phi}{k_p + 2k_f - (k_p - k_f)(1 + \gamma)^3\phi}$$

.....(10)

7- Jang and Choi [47]:

$$k_e = k_f(1 - \phi) + k_p\phi + 3C \frac{d_f}{d_n} k_f Re_{d_p}^2 Pr \phi$$

.....(11)

From these models we conclude that the effective thermal conductivity depends on the thermal conductivity of the nanoparticles, the thermal conductivity of the base fluid, the partial volume fraction and the size of the particle. Also, we can conclude that the thermal conductivity of ferrofluids is closely related to the thermal conductivity of the base fluid.

Since ferrofluids are nanofluids with iron nanoparticles, their physical properties differ considerably depending on the base fluid used. For example, oil based ferrofluid has the same greasy texture as oil. The water based ferrofluid has a dark black color and can be washed away easily by tap water. The main components of water based ferrofluid are [48]:

Table 1: Typical Components of Water Based Ferrofluid

Magnetite	1-4 % by volume
Water Soluble Dispersant	7-27 % by volume
Water	69-92 % by volume

It was later shown by experiments that this kind of ferrofluid dries quickly (in one to four hours) since water is the base fluid. Figure 8 shows oil and water based ferrofluids:

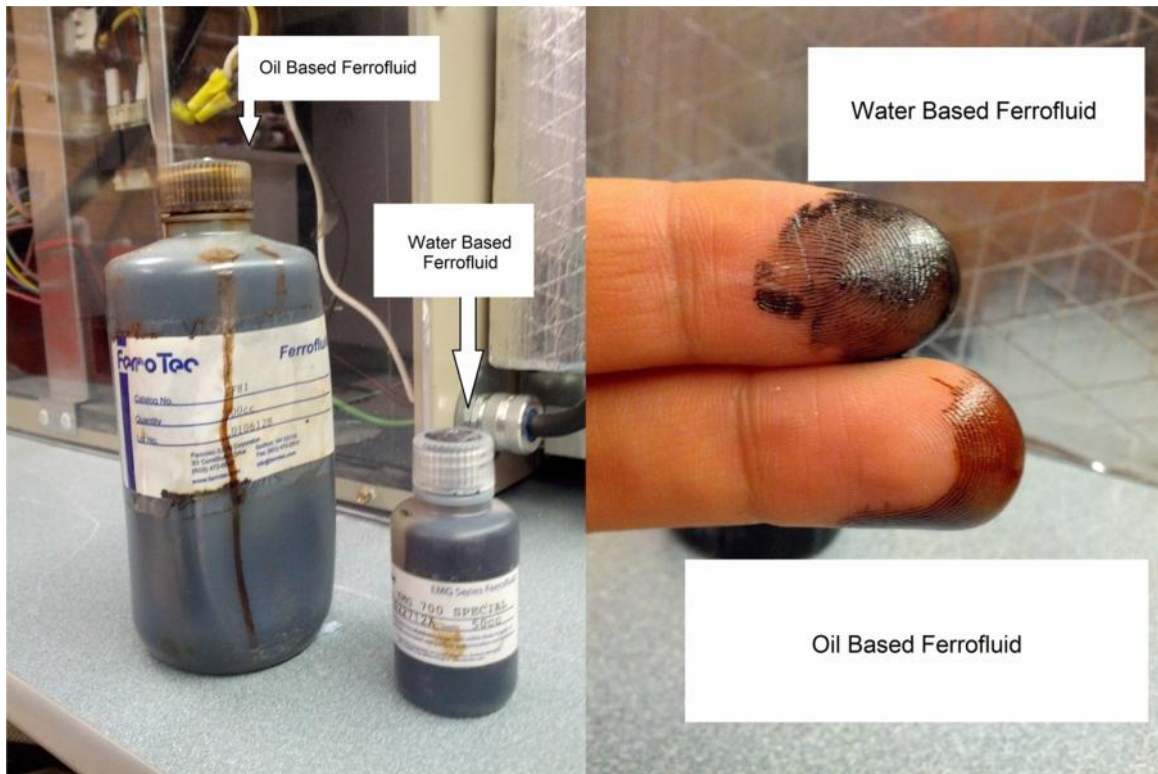


Figure 8: Oil and Water Based Ferrofluids

The second type of ferrofluid that has been studied is the oil based. The oil based ferrofluid is thicker than the water based and has a brown color. This kind of ferrofluid cannot be washed away by tap water, since it is oil based. It is hard to clean but can be wiped out with a piece of cloth. Table 2 shows the main components of such kind of fluid [49]:

Table 2: Typical Components of Oil Based Ferrofluid

Magnetite	3-15 % by volume
Oil Soluble Dispersant	6-30 % by volume
Oil:	55-91 % by volume

Oil is a chaotic material. In other word, it can adhere to the surface in contact but it can be wiped as mentioned above. In general, one advantage of ferrofluids in the context of being interface materials is that they can be held in place with magnets.

1.7 Synthesis of Ferrofluids

Ferrofluids can be manufactured through a variety of methods such as co-precipitation of metal salts [50], reduction in aqueous solution [51, 52], reduction in reverse micelles [53-56], and reduction of organometallic precursors with H₂ under mild conditions [57-59], and synthesis in organic media using Fe_xPt_x [60]. The latter method will be explained in detail as an example for ferrofluid manufacturing.

In this method, i.e. the synthesis in organic media using Fe_xPt_x, 0.5 mmol of platinum acetylacetonate and 1.5 mmol of 1,2-hexadecandiol are dissolved in 20mL of dioctyl ether in vacuum chamber and then heated up. When the solution reaches 100 oC, 0.5 mmol of Oleic acid, 0.5 mmol of oleylamine, and 0.5 mmol of iron pentacarbonyl are added to the solution. After that, the solution is heated further to 287-288 °C and boiled in a vessel attached to a condenser, so that the vapor condenses and flows back into the vessel. This process lasts for thirty minutes. Then, the

nanoparticles will be ready after cooling down the solution to room temperature [60, 61].

After the synthesis process, the washing process starts. The nanoparticles should be washed several times to eliminate the excessive surfactant from the mixture. In order to do so, 40 mL of ethanol should be added to the solution, which will cause the nanoparticles to precipitate under the effect of centrifugation. Consequently, the supernatant can be eliminated. The next step is to redisperse the nanoparticles in 20 mL of Hexane, 0.05 oleic acid and 0.05 mL of oleylamine. The washing process should be repeated several times [60]. The next step after removing the supernatant is to disperse the nanoparticles in a mixture of 2 mL of TMAOH (10 wt % in H₂O)[62-64] and 100 mL of deionized water. The mixture will be shaken well for five minutes using ultrasound energy. Again, the mixture will be centrifuged to eliminate the excess of surfactants. The wet residual solids will be remixed with TMAOH solution (0.01 wt %) as desired to obtain the required concentration [60].

1.8 The RevCon Challenge

As mentioned earlier in chapter one, many organizations showed interest to modify or find an alternative to the wedgelock design due to its high thermal resistance. In the fall of 2011, the Office of Naval Research (ONR) and the Defense Advanced Research Projects Agency (DARPA) announced the first RevCon Challenge to seek a novel design for a field reversible thermal connector. After submitting proposals,

University of Missouri-Columbia team was notified of their selection as one of four competing teams in the challenge.

After funds became available, our team started building the prototype. The main idea of the design was to use the aforementioned water based ferrofluid as interface material between the contact surfaces. The competition required teams to use Aluminum (AA6061) instead of a printed circuit board and attaching a copper rail to the card. The team modified the original cooling block and copper rail. The design also utilized neodymium magnets to keep ferrofluid in place. The final design is shown below in figure 9:

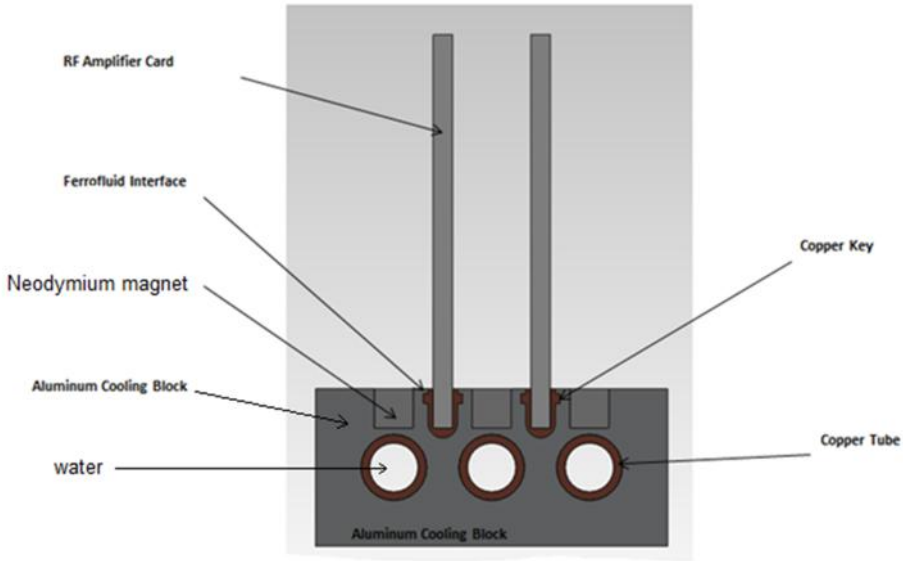


Figure 9: The RevCon Design

After submitting the prototype to ONR, University of Missouri team travelled to the Applied Physics Laboratories at the John Hopkins University near Laurel, MD to test

their device. The device measured the second lowest thermal resistance and the team won the most creative design prize [65].

1.9 Motivation after RevCon Challenge

Although the RevCon design scored low thermal resistance at the test site, there were many issues that needed to be taken care of: First, the thermal resistance of the system was not stable for unknown reasons. Second, the analytical calculations did not meet the experimental results, and finally there was no method for wiping or cleaning cards upon removal from the system. Thus, there was motivation to optimize this design, and this inspired the thesis.

1.10 Goals to accomplish

The wedgelock design that is currently being used to mount and dismount electronic cards from cooling blocks or chasses has multiple issues: First, the heat transfers from cards to cooling blocks through one side only. In other words, the wedgelock itself has high thermal resistance since it is hollow. Second, the type of contact is dry, which means that there are interstices filled with air.

As a result, a new design that solves these issues and provides lower thermal resistance is wanted. The Defense Advanced Research Projects Agency (DARPA) and the Office of Naval Research (ONR) have both shown interest in developing a better thermal connector. This thesis describes analysis of a novel type of such connector based on a magnetically controllable nanofluid.

The analyses that have been done can be summarized below:

- 1- Experimental Analysis
- 2- Mathematical Analysis
- 3- Numerical Analysis
- 4- Magnetic Analysis

CHAPTER TWO- EXPERIMENTAL SETUP

2.1 Introduction

As stated before, the Ferrofluid design has a lower thermal resistance than the wedgelock design; however, there were some issues such as the mismatch of analytical with experimental data, unstable thermal resistance and the absence of a fluid wiping technique.

In this chapter, the problem will be discussed in details; the new experimental setup and the reason for such modifications will be explained.

2.2 Post RevCon issues and analysis

The RevCon design requires heat to be transferred from the aluminum card to the copper rail, which is attached to the card through soldering. Figure 10 shows the results of the RevCon team. The thermal resistance for the both designs is shown.

According to Fourier Law of heat transfer:

$$R_{th} = \frac{\Delta T}{Q}$$

.....(12)

ΔT is the temperature difference between the card and the cooling block while Q is the input heat to the system. For the wedgelock design, the thermal resistance R_{th} should be constant. However, we can notice that the thermal resistance is decreasing with higher power input. The Law of thermal expansion explains this behavior very well:

$$\Delta V = V\alpha_V\Delta T$$

.....(13)

ΔT represents the temperature difference between the initial temperature (card is cold) and the final temperature when measurement was taken. Thus, the new volume is $V+\Delta V$. As the card expands when it gets hot, the gap between the card and the cold block should get smaller, meaning the thickness of the ferrofluid should get smaller, and hence the thermal resistance should get smaller like in the wedgelock design. But the data does not support that trend. Contact pressure does not play any role when talking about the water based ferrofluid. See equation (22) by Yovanovich [20] (chapter four).

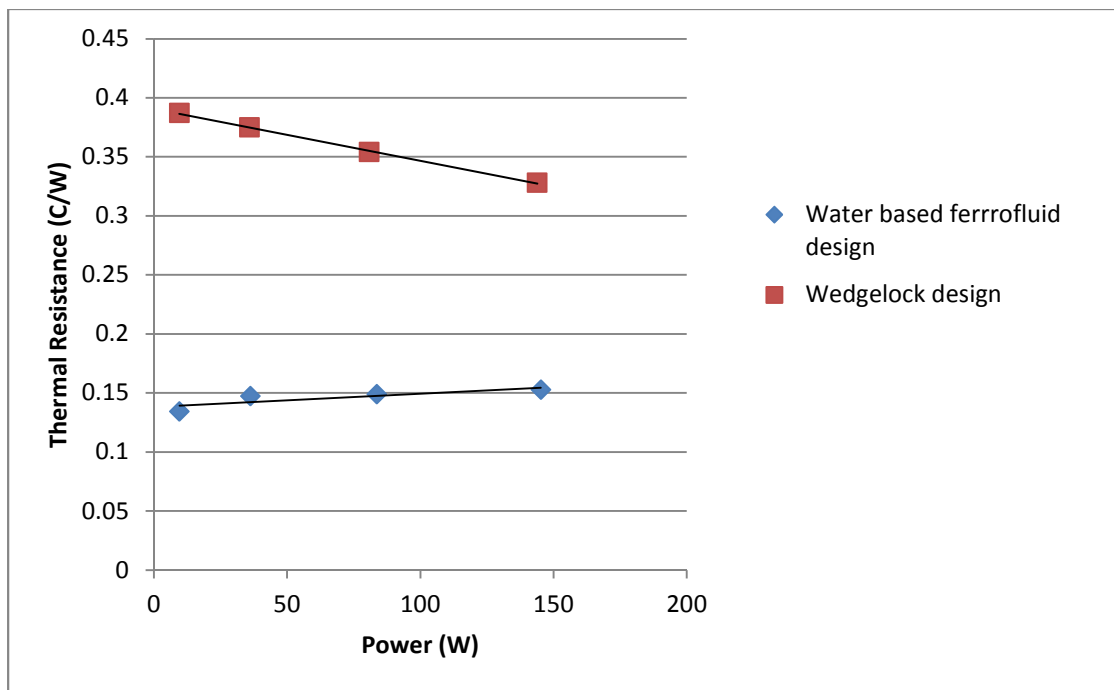


Figure 10: Thermal Results of RevCon Analysis

After performing the same experiment three times, the exact same results were obtained. Thus, the probability of random occurrence was eliminated. The solder

interface between the copper rail and aluminum card was unfortunately confounding the data. The solder material has unknown thermal conductivity, and the soldering process was done unprofessionally, which means that there might be some air bubbles or gaps in the solder that could affect the contact resistant between the rail and the aluminum card. Considering all the above issues, it was decided to machine a new card entirely out of Aluminum to eliminate the soldering material and that interface so that the ferrofluid interface could be studied more carefully with the new card design. The new card consisted of one piece of Aluminum 6061 that included the shape of the metal rail so that it could slide into the cooling block. The manufacturing process for the new card is explained in detail with dimensions in appendix A. Figure 11 below shows the Aluminum card compared to the Copper-rail card, with the copper rail is partially removed from the card, from the RevCon design:

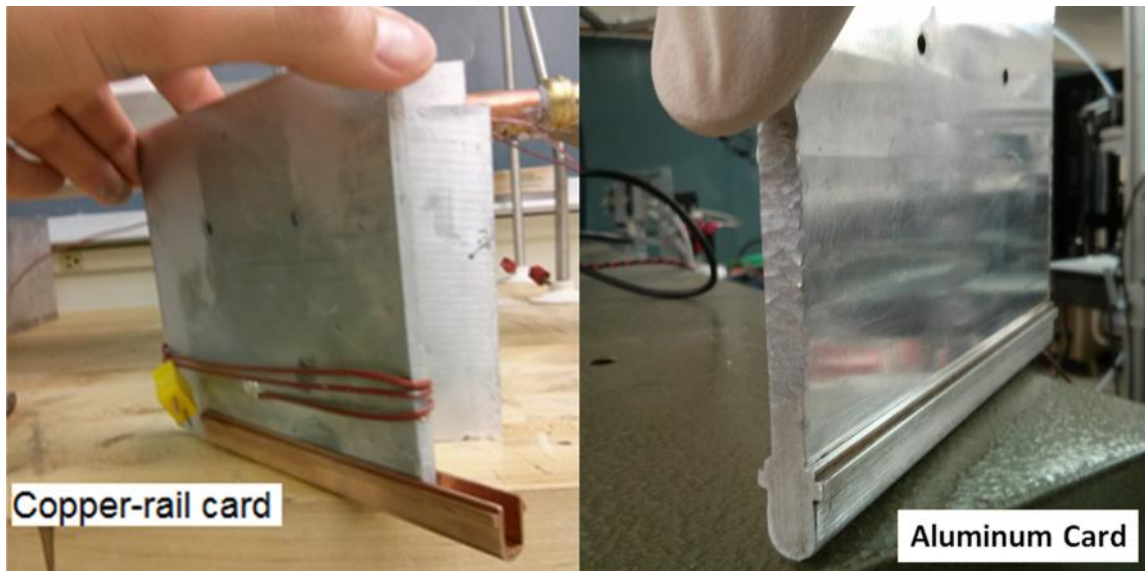


Figure 11: Copper-rail Card and Aluminum Card

2.3 Installing the Heat Source and Thermocouples

In this experimental setup, LPS 300 Vishay power resistor has been used as a heat source (Figure 16) because of its high power (300 Watts), which can generate a lot of heat. EVGA frostbite thermal paste has been used as thermal interface material between the card and the power resistor because of its high thermal conductivity of 6.5 W/m.K. To attach the power resistor to the card, two holes had been drilled in the card using a commercial drill press and the power resistor had been attached using two regular screws. The final setup can be seen in Figure 12:



Figure 12: The final setup for the card

Two type k thermocouples were used in the system to obtain temperature values. K-type thermocouples were chosen because of their low price and wide range of measurement ($-200\text{ }^{\circ}\text{C} - 1250\text{ }^{\circ}\text{C}$), according to the manufacturer [66]. One thermocouple was attached to the card at 0.9 inch from the lower edge of it to

measure the temperature right before the interface, and the other thermocouple was attached to the lower half of the cooling block, sandwiched between the two halves to measure the temperature of the cooling block. Both thermocouples were attached using Arctic Silver solder paste because regular solder cannot stand the high temperatures that are expected during the experiments. Figure 13 shows thermocouples. One is attached to the card and the other is attached to the cooling block:

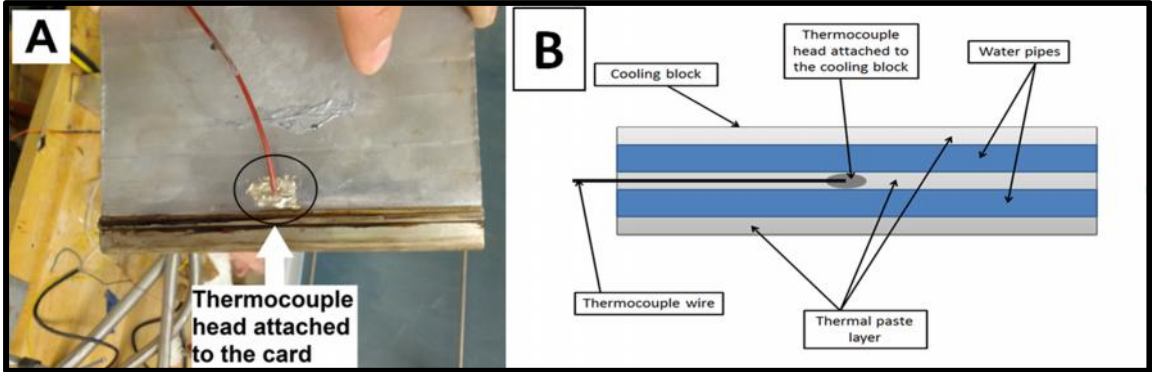


Figure 13:(A): Thermocouple Attached to Card Using Solder Paste.

(B): Thermocouple Attached to Cooling Block Using Same Solder Paste.

2.4 Installing the Magnets

Two rows of neodymium NdFeB 52 magnets are used to keep the ferrofluid in place (see figure 14 and 20). Otherwise, ferrofluid spills out of the cooling block due to engaging and disengaging the card besides the effect of gravity. This kind of magnets was used because of its high magnetic power density, inexpensive price and low

volume to field strength ratio [67]. These magnets measured 0.25 in × 0.5 in × 2 in each. The length of each magnet is 2 inches, so three magnets were used in each row to accommodate the length of the card.

The magnetic flux intensity B can be found through the following relation [67]:

$$B = \mu_0 (H + M) \quad \text{.....(14)}$$

Where H is the magnetic field intensity, M is the magnetization and μ_0 is the magnetic permeability of free space, which is $0.4\pi \times 10^{-6}$ Henry/m.

The magnetic force can be expressed as:

$$force = \frac{A B^2}{2\mu_0} \quad \text{.....(15)}$$

B is the magnetic flux density and A is the cross sectional area of the area through which the magnetic flux is passing. The figure below shows the magnets after installation:

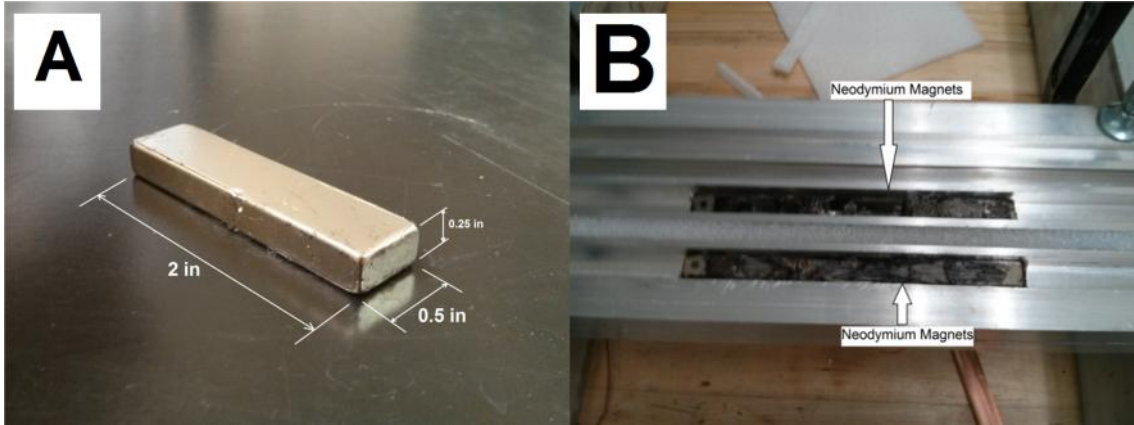


Figure 14: (A): A Single Neodymium Magnet

(B): Magnets Installed in the Cooling Block

It is good to mention that the distance between the magnets, which is 1.251 inches, has already been optimized by the RevCon team. However, the intensity of the magnets was not optimized. It is well known that electronics and magnets have some interaction with each other. As a result, the lowest magnetic field to hold the ferrofluid in place should be investigated. A detailed magnetic analysis will be presented in chapter seven.

2.5 Installing the wiping material

Whenever the card is removed, some of the ferrofluid may stay coated on the card, which is not preferred and requires removal. One of the easiest methods to remove the ferrofluid from the card is wiping it. The wiping method that has been used consists of rubber material in the shape of the rail and a supporting plate. This wiping assembly can be attached to both ends of the cooling block via screws or epoxy. Thus, the card will be wiped clean upon removal from the cooling block. The assembly is shown in figure 15:

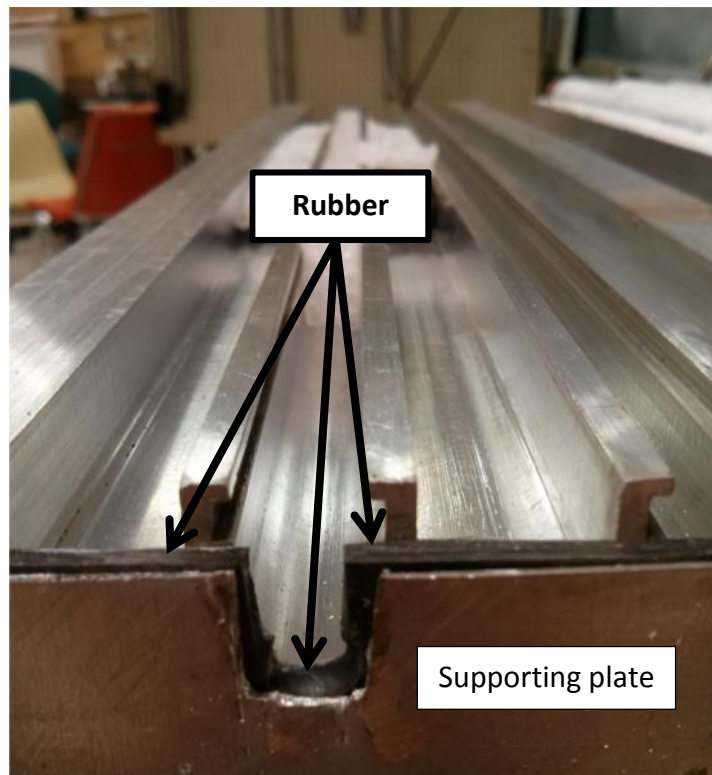


Figure 15: Wiping Assembly

Upon experiments, the wiping method demonstrated outstanding cleaning for the card edges, given the basic cutting method. In figure 16 below the card is shown before and after being wiped by the assembly:

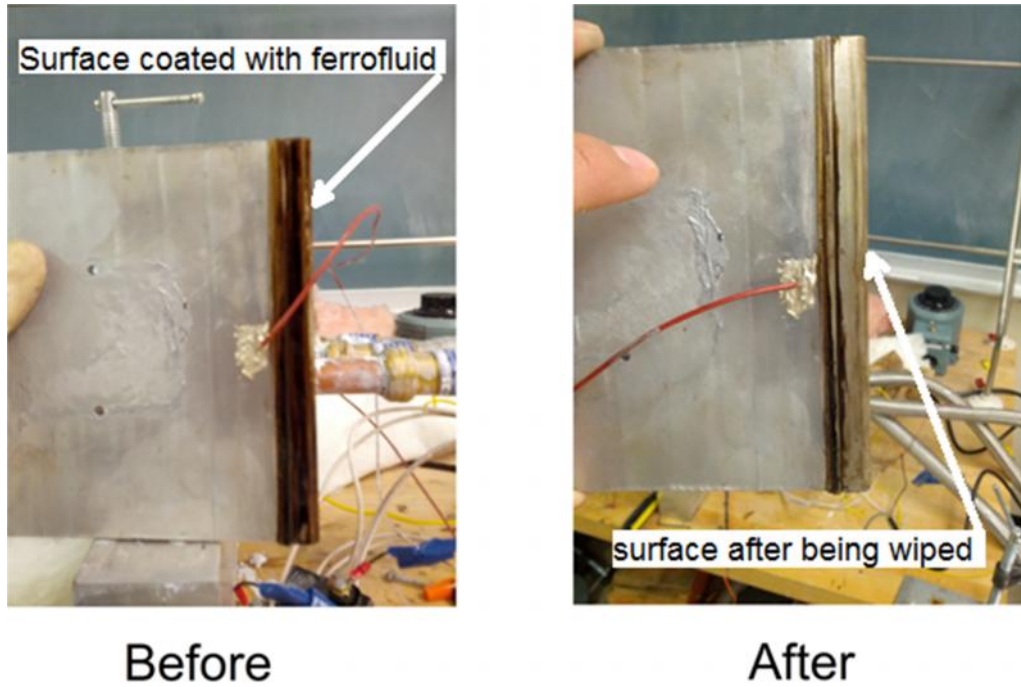


Figure 16: Card Before and After being Wiped

Thus, the card can be kept clean upon removal from the cooling block by installing a rubber flap on the end of the cold block. The retained ferrofluid will stay in the card channel because of the rubber flap and will return to its original place because of the attraction of the magnets.

2.6 Cooling Block setup

The cooling block setup involves putting the cooling block halves together after applying some thermal paste on and between the channels to maximize the heat transfer. Both halves of the cooling block are made of aluminum alloy 6061. Figure 17 shows the two halves of the cooling block:

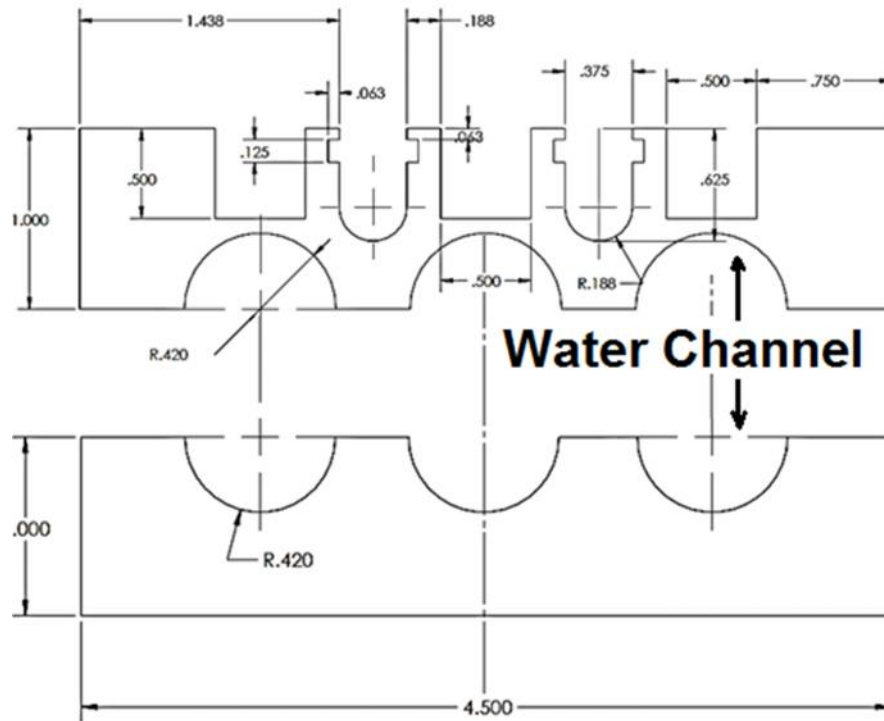


Figure 17: Cooling Block Dimensions

Three copper pipes were installed in the water channels shown in the figure above. The purpose of these pipes is to transfer heat from the cooling block to the water by conduction. Copper was chosen because of its high thermal conductivity of $401 \text{ W/m}\cdot\text{K}$. Figure 18 shows these pipes:



Figure 18: Cooling Block with copper pipes installed

The cooling block halves are held together using C-Clamps. Next, one side of the pipes is connected to tap water source for cooling while the other side is connected to the drain hose. Figure 19 below shows the cooling water setup:

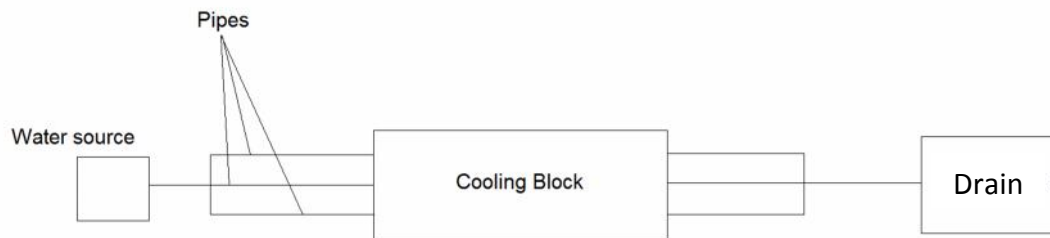


Figure 19: Cooling System Setup

2.7 Thermocouples and Electrical Setup

The power resistor (heater) is connected to both a variable power source in order to supply different voltages and to the computer interface in order to obtain real-time measurements of the voltage. The electrical circuit included a shunt resistor of 0.01 Ohms so that the value of power could be found. Figure 20 shows the electrical circuit for the heater:

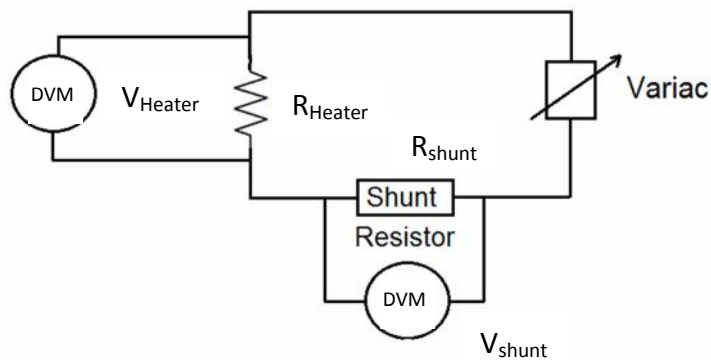


Figure 20: Heater Electric Setup

The shunt has a known resistance of 0.01 Ohm. By measuring the voltage across the shunt, it is possible to find the circuit current according to Ohm's law:

$$I = \frac{V_{shunt}}{R_{shunt}}$$

.....(16)

Since the voltage across the power resistor (heater) was measured, the power can be found:

$$Power = \frac{V_{shunt}}{R_{shunt}} \times V_{Heater}$$

.....(17)

It is good to mention that the voltages were measured using a Keithley 2701 digital multimeter with data logger. Also, the same device was used to obtain the temperature from the thermocouples and from an Omega Ice Point device, which was also installed and connected to the computer interface to measure the ice point voltage in real time to help calculating the temperature of the card and the cooling block. Thus, all measurements were carried out in real-time and simultaneously. Finally, the card was insulated so that heat transfers to the cooling block by conduction, which reduces the effect of convection and radiation.

The setup of the device is shown below:

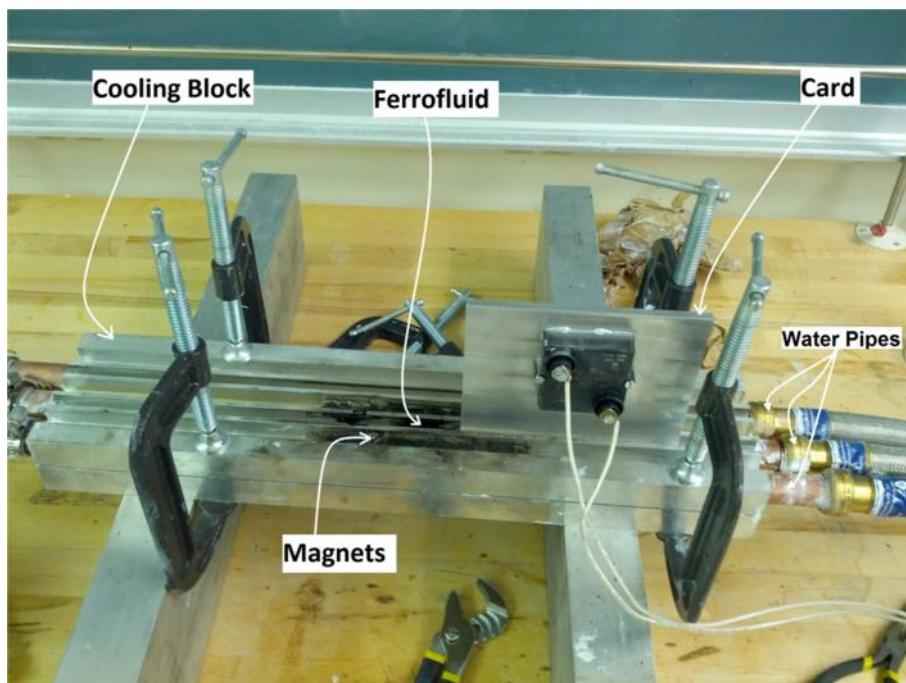


Figure 21: The Device with the Ferrofluid Design Card Attached

CHAPTER THREE – EXPERIMENTS AND RESULTS

The goals of the experiments were to answer the following questions:

- 1- Why is the thermal resistance not stable?
- 2- If we use a card made of aluminum, is it possible to match between analytical results and experimental results?

After the new card was ready, the same experiment done by RevCon team was performed again but with the new card in order to see if the problem was in the soldering material.

The experiment was performed for different powers: 9.5, 36.5, 83.5 and 145 Watts. Also, for each power ten minutes was allowed to elapse before taking the measurements so that the system would reach a steady state. The following results were obtained:

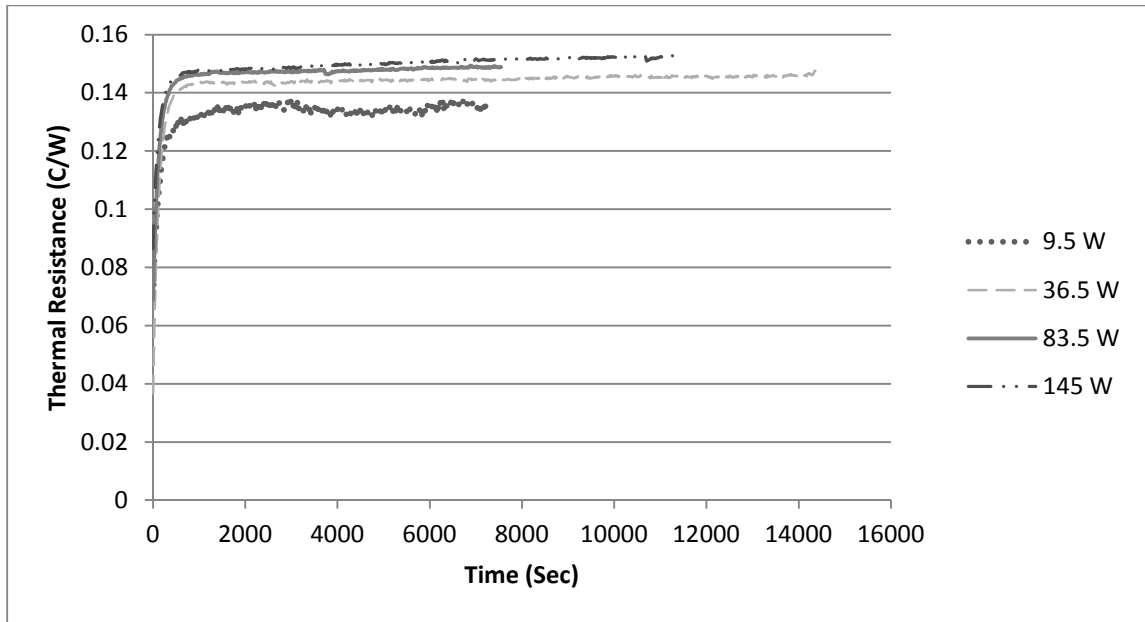


Figure 22: Thermal Resistance Versus Time for Water Based Ferrofluid for aluminum card

From Figure 22 we can notice that the thermal resistance is not stable and is constantly increasing. Also, the higher the power is, the higher the thermal resistance goes, noting that the experiments were run from low power to high power. The same experiment was carried out three times and the same results were obtained. This behavior might be due to incorrect measurements, which means that more time is required to reach a steady state condition. In order to solve this issue, a long experiment was carried out, in which the device was run for approximately thirteen hours at 36.5 Watts input to locate the steady state time. However, this experiment was not successful and there was no steady state point identified. The same experiment was repeated, and the exact same results were obtained. Figure 23 shows the long experiment that was mentioned earlier. From figure 23 it is clear that the system did not reach a steady state. Since the thermal resistance is continually

increasing and the solid aluminum card thermal resistance should be almost constant, then the interface must be degrading. The magnets are holding the ferrofluid with its particles in place. Also, we know that the number of particles is not changing. Thus, we conclude that the liquid must be changing and evaporation is a likely phenome. Card inspection revealed that the ferrofluid was completely dry, which supports this hypothesis. Also, examining figure 23, we can easily notice that the thermal resistance is not reaching a steady state and keep increasing when the power increases, which means that the original problem is not solved yet and the issue is not with the soldering material itself.

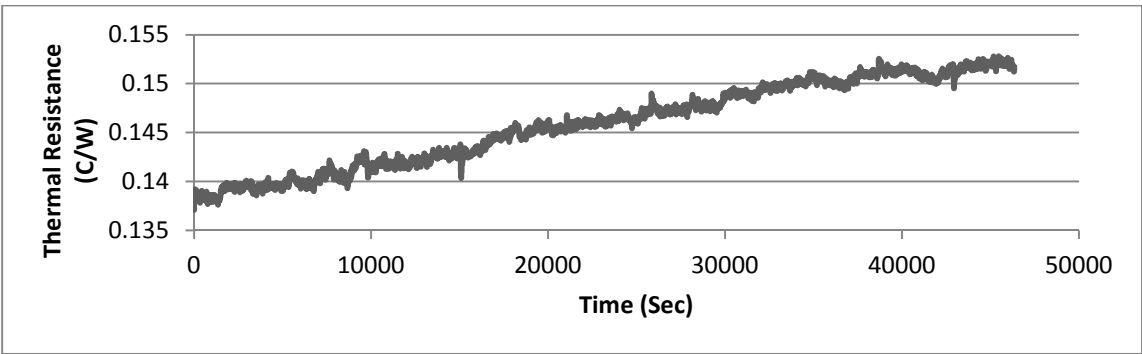


Figure 23: Thermal Resistance Versus Time for Stability Check (Water Based Ferrofluid)

To test the hypothesis that the water was evaporating, an oil based ferrofluid was tested, as the oil carrier should not evaporate. Before power varying experiments with oil based ferrofluid, it was important to perform a stability check. A twelve hour experiment was performed at 36.5 Watts, the result is shown figure 24:

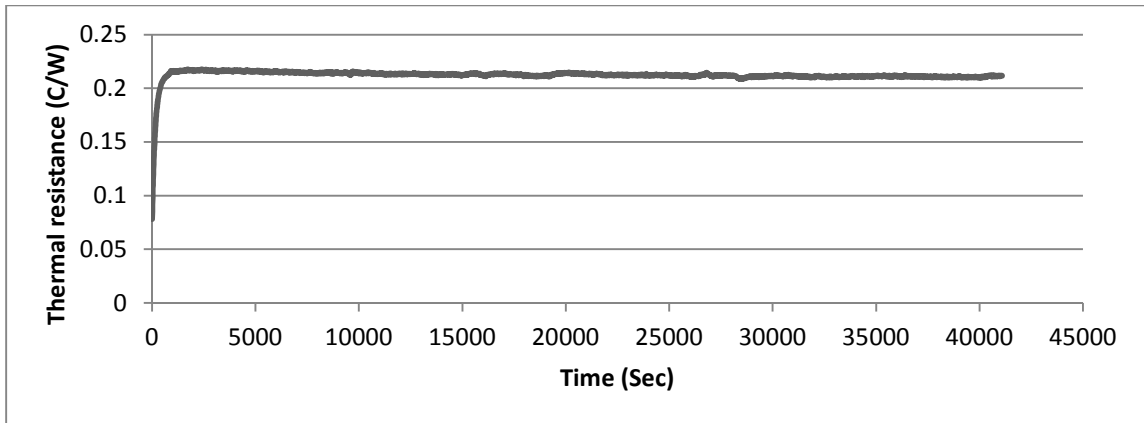


Figure 24: Thermal Resistance Versus Time for Stability Check (Oil Based Ferrofluid)

As we can see, the oil based reached to a steady state condition after less than one hour and remained at the same value. Also, a repeated experiment yielded the same results. Thus, oil based ferrofluid appears to be stable compared to water based ferrofluid.

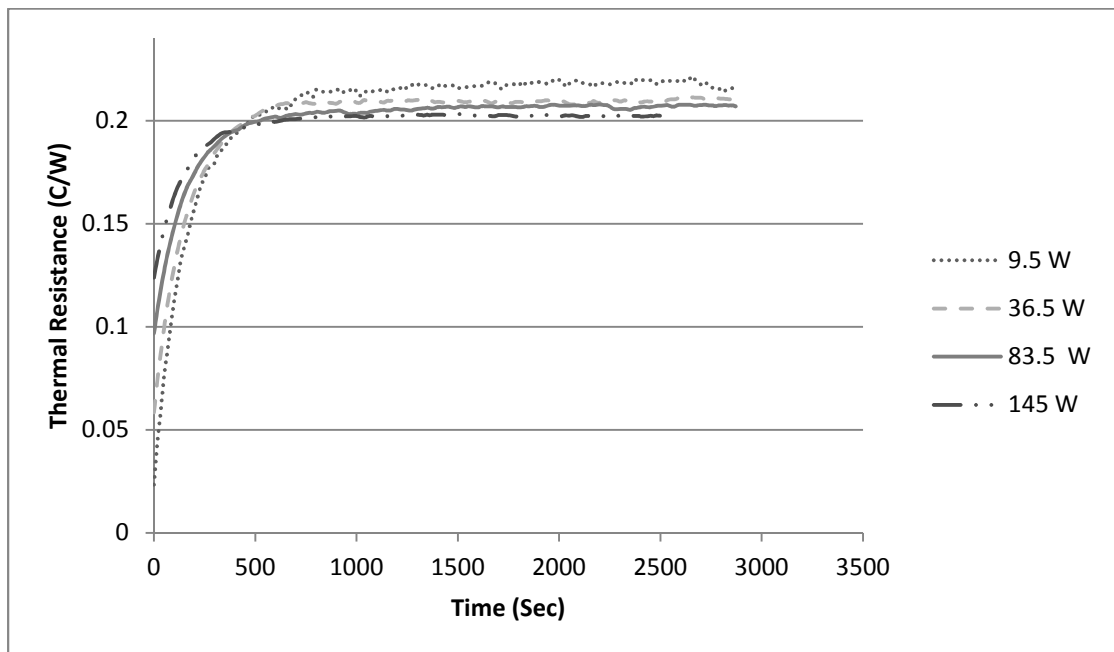


Figure 25: Thermal Resistance Versus Time for oil Based Ferrofluid For Aluminum Card

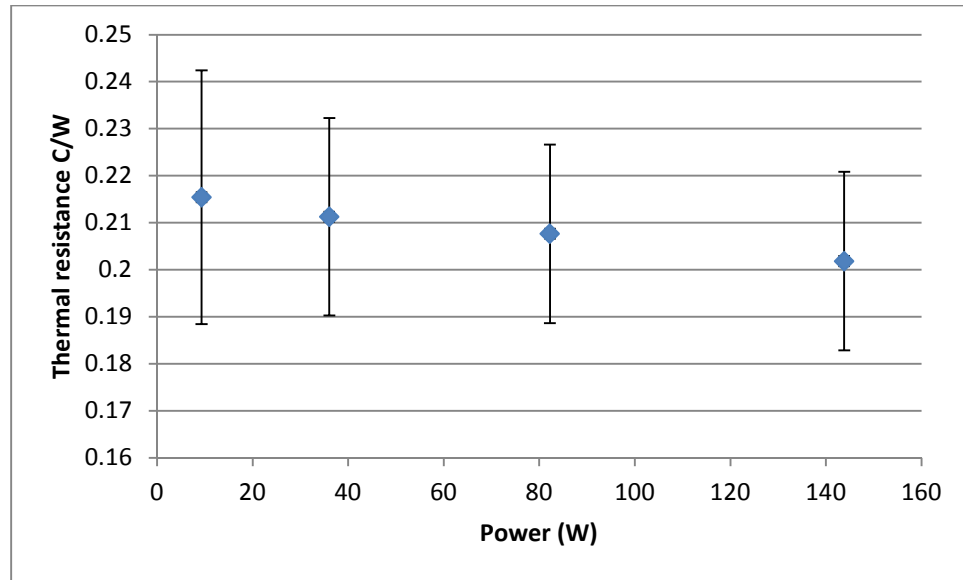


Figure 26: Thermal Resistance versus Power (Oil Based Ferrofluid)

As we can see in figures 25 and 26, the thermal resistance decreases whenever the power increases. This behavior is due to thermal expansion, recalling that $\Delta L = \alpha \Delta T L$ where ΔL is the expansion of the aluminum card and ΔT is the temperature rise above the ambient. In figure 27, it is noted that an expansion of the card will reduce the interfacial gap causing higher contact pressure.

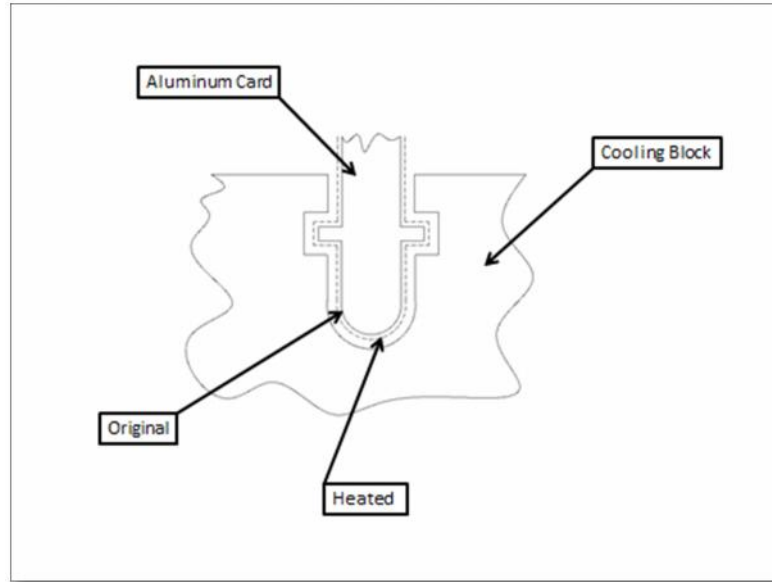


Figure 27: Card before and after heating

Thus, analyses for wedgelock design may help us better understand this behavior since the wedgelock is the baseline for comparison. A new experiment must be performed for the wedgelock design, starting with a study to find the steady state point for that design. Again, after performing the same experiment twice, the result is shown in figure 28:

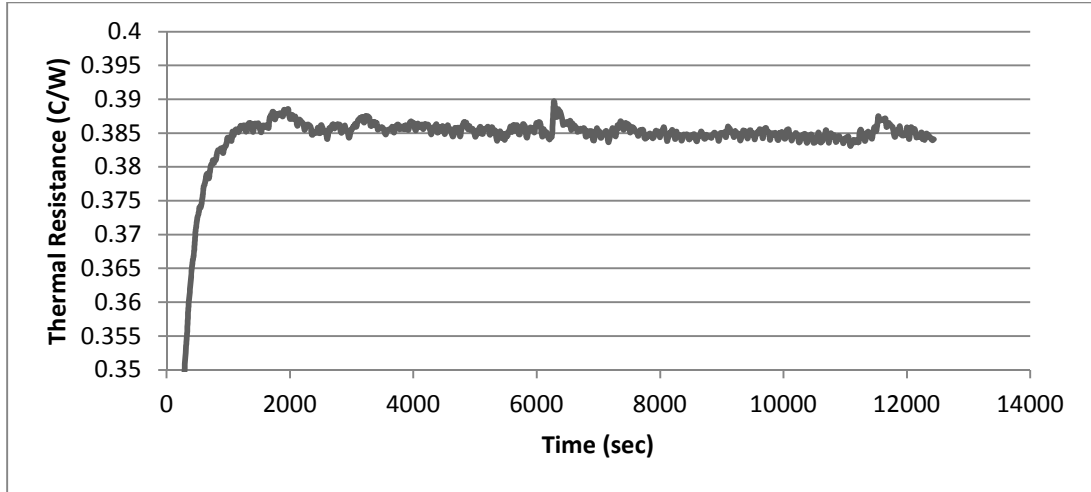


Figure 28: Thermal Resistance Versus Time for Stability Check (Wedgelock Design)

Since we know now that the wedgelock design’s thermal resistance appears stable, we can run experiments for it at 9.5, 36.5, 83.5, 145 Watts respectively:

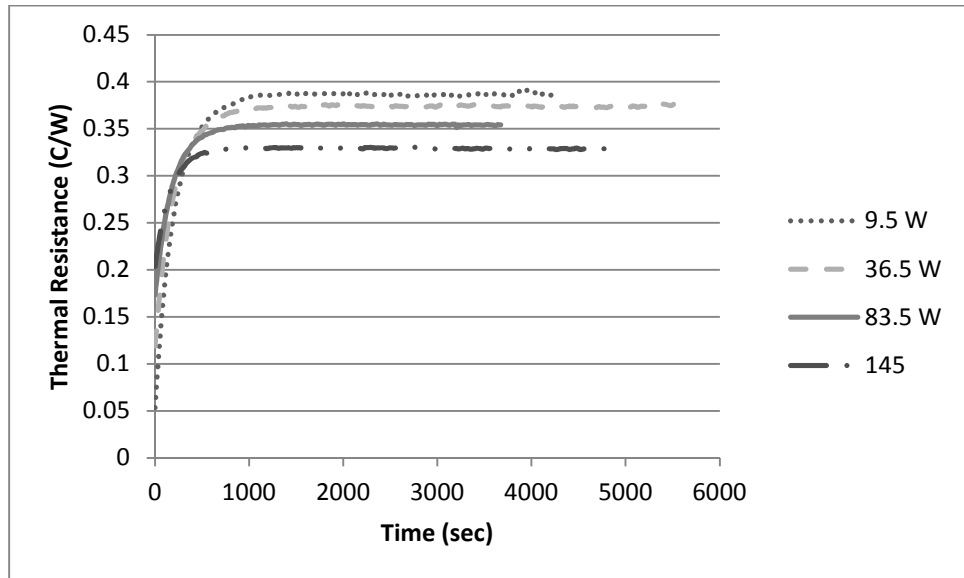


Figure 29: Thermal Resistance Versus Time for wedgelock design for Aluminum Card

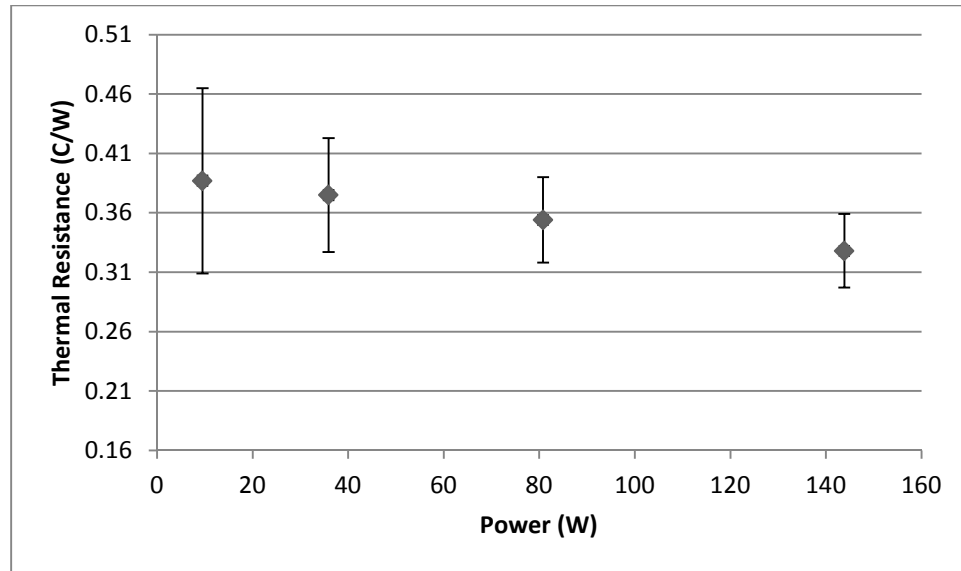


Figure 30: Thermal Resistance versus Power (Wedgelock Design)

From figures 29 and 30, it is obvious that the thermal resistance decreases when the power increases. In the case of the wedgelock, however, the expansion of the aluminum card increases the contact pressure, and therefore reduces the thermal resistance as suggested by the Yovanovich contact resistance model (see section 4.2). The figure below compares wedgelock design, water based ferrofluid design, and oil based ferrofluid design for the four different powers:

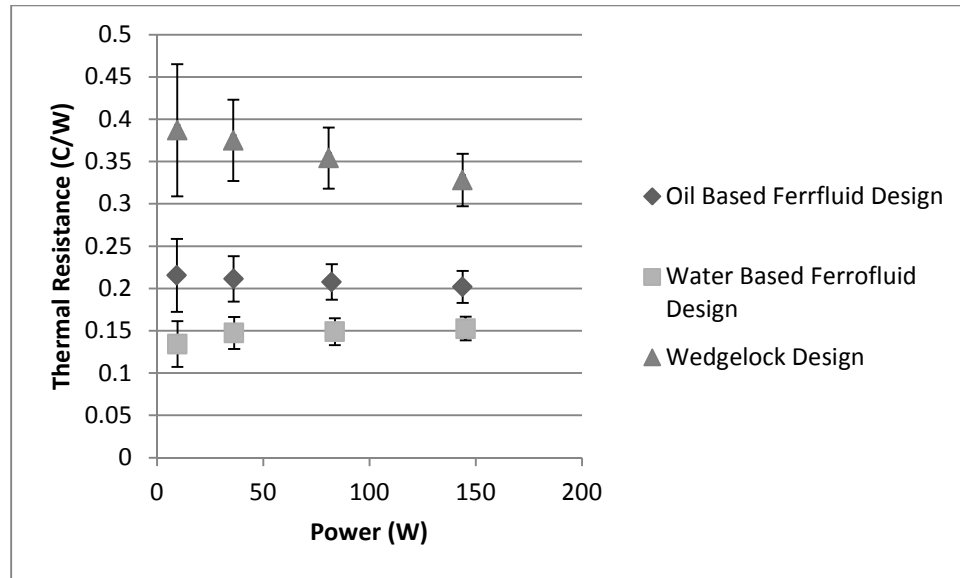


Figure 31: Oil Based Ferrofluid Design, water based ferrofluid design and Wedglock Design

Figure 31 shows very well that the wedglock design has the highest thermal resistance. Upon contacting the manufacturer of the wedglock, it was found that wedglocks have very high thermal resistance and it is not expected that any heat can transfer through wedglocks. Since there is no pressure applied to the bottom of the card, most of heat transfers through one side of the card, which explains the high thermal resistance according to the thermal resistance equation $R_{th} = x/kA$. It is very clear that using water based ferrofluid has the lowest thermal resistance. Unfortunately, the water based ferrofluid may not be the best solution from a stability standpoint; the oil based fluid, on the other hand, has a resistance that is about 1.5 times larger than the water based fluid but appears stable over extended testing. It also shows slight improvement as the heating increases.

Relative to the reference wedgelock, the oil based ferrofluid interface shows a thermal resistance that is 1.8 times lower. While this is a significant solution in the thermal contact resistance it is not as large as desired. To improve the interface further, a modeling study was carried out to better understand the heat transfer process from the card to the cold block.

CHAPTER FOUR – ANALYTIC MODELING OF THE SYSTEMEM

In this chapter, an approximate mathematical approach will be developed to estimate the thermal resistance of the interface. The purpose of this analysis is to estimate the film thickness of the ferrofluid, and to find its effect on the thermal resistance, and also to study the wedgelock heat transfer.

4.1 Ferrofluid design

From the experimental results, the cooling plate temperature at the cooling plates will approach the cooling water temperature (around 21.1 C).

It is known that the thermal conductivity for Aluminum Alloy 6061 is 167 W/m.°C. Also, after contacting Ferrotec Inc. , the manufacturer of the ferrofluid, the thermal conductivity for the ferrofluid was found to be 0.158 W/m.°C. Figure 32 below shows the system to analyze:

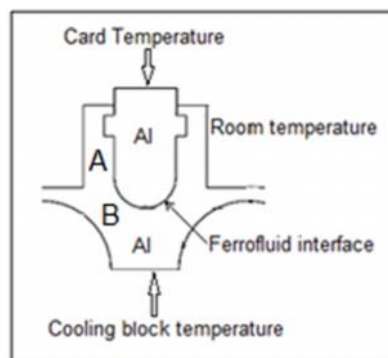


Figure 32: System to Analyze

Since the walls have almost the same thickness, an easier equivalent shape will be studied instead. This shape is shown in figure 33:

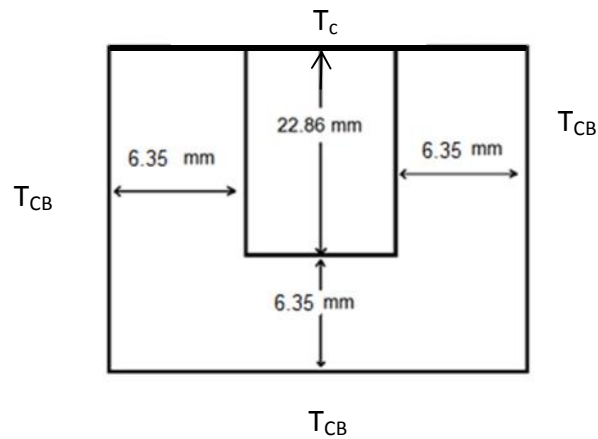


Figure 33: Equivalent Shape

It was found that the distance between the thermocouple and the edge of the card is around 0.9 inches or 22.86 mm. On the other hand, the wall thickness was averaged as 0.25 inches, which is the average of the wall thickness A and B, where A is 0.2 inches and B is 0.3. Also, it is good to mention that the face of the cooling block and the card are thermally isolated. So, heat is transferred by conduction only to the cooling block. With respect to the ferrofluid film, there is no heat transfer by convection through it since ferrofluid is kept in position by magnets and it forms a stagnant thin film. Thus, the ferrofluid layer can be assumed to transfer heat by conduction only.

Figure 34 shows an electrical equivalent scheme for the thermal resistance:

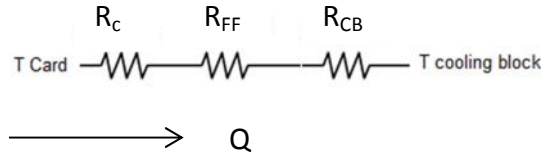


Figure 34: Electrical Equivalent Scheme

Where T_{card} represents the measured temperature on the card using a k type thermocouple, $T_{cooling\ block}$ is the temperature of the cooling block also measured using a k type thermocouple.

So,

$$R_{th} = \left(\frac{x}{kS}\right)_{card} + \left(\frac{x}{kS}\right)_{Ferrofluid} + \left(\frac{x}{kS}\right)_{cooling\ block} \dots\dots\dots(18)$$

Where S is the geometry shape factor, shape factors depend on the shape of the wall. The following shape factors will be used[68]:

1- For the card:

$$S = \frac{2}{L\pi} \sum_{n=1}^{\infty} \frac{2[(-1)^n - 1]}{n} \tanh \frac{n\pi W}{L} \dots\dots\dots(19)$$

Where L is the width of the card and W is the height of the card as shown in figure 35:

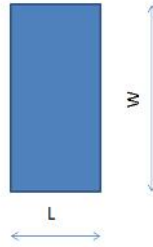


Figure 35: Card Shape factor details

2- For the ferrofluid film:

$$S = \frac{2\pi L}{0.785 \ln \frac{w+x}{w}}$$

.....(20)

Where x is the film thickness and w is the width of the card as in figure 36:

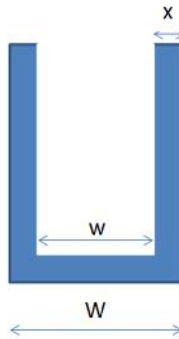


Figure 36: Ferrofluid shape factor Details

3- For the cooling block:

$$S = \frac{2\pi L}{0.930 \ln \left(\frac{W}{w} \right) - 0.05}$$

.....(21)

W represents the outer width and w is the width of the channel as shown in

figure 37:

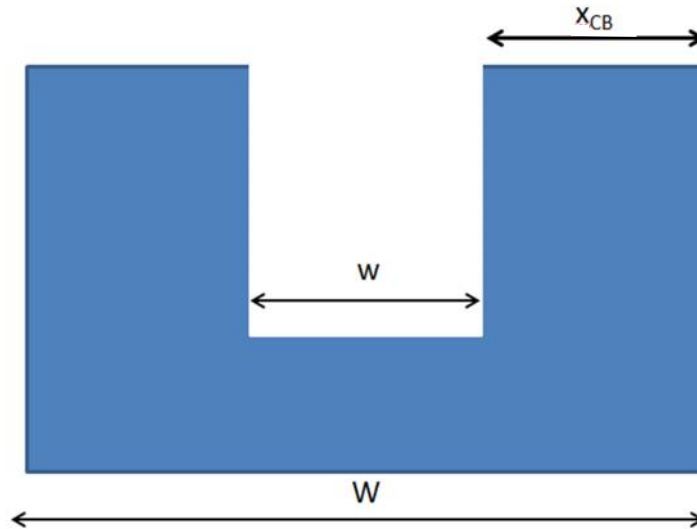


Figure 37: Shape factor details for Cooling Block

Substituting the aforementioned dimensions into equation (18):

$$R_{th} = 0.12 + \frac{x \ln \frac{w + 2x}{w}}{1.21 k_{ff}}$$

.....(22)

Where k_{ff} is the thermal conductivity of ferrofluid, supplied by the vendor. The equation above explains the relation between the thermal resistance and the gap clearance. Figure 38 was created by plotting equation 22 and varying x

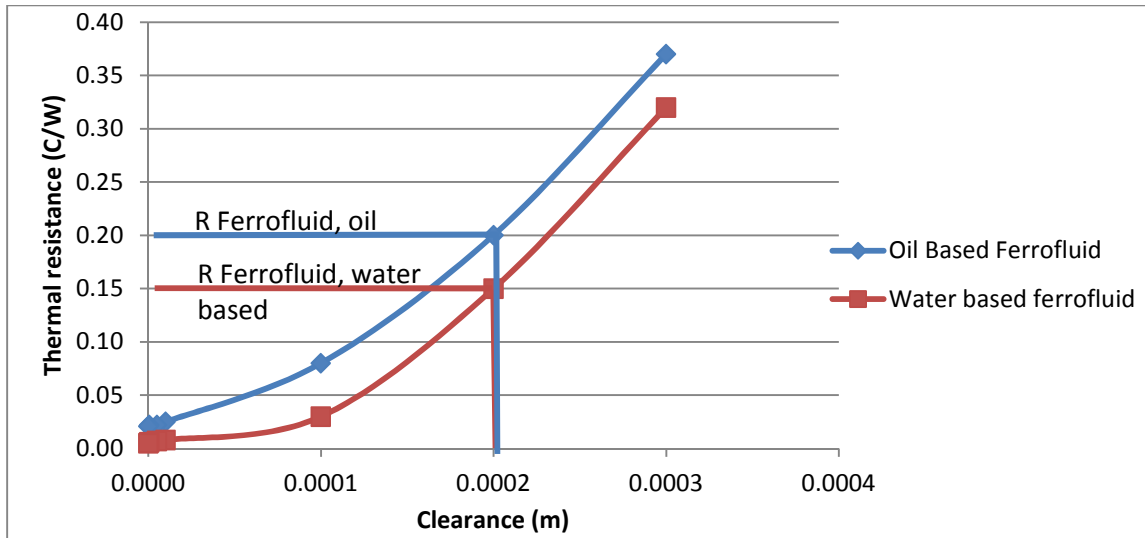


Figure 38: Thermal Resistance Versus Clearance

Noting the values of the thermal resistance from the experimental data, we learn that the gap between the card and the cooling block is approximately 0.2 mm for both oil and water based designs.

From the figure above, we conclude that the relation between the thermal resistance and the clearance between the card and the cooling block is proportional as was expected. These results support our claim about the thermal resistance in the oil based ferrofluid design and the wedgelock design that was mentioned earlier in chapter three. Also, we can conclude that the smaller the gap is, the lower the thermal resistance is. However, there are some limitations:

- 1- Machining limitations: it might be expensive and or difficult to machine smaller clearances.
- 2- Easiness of disengaging: It might be difficult to remove the card if the gap is very small because of the expansion of the card which might require a lot of

time to wait for the card to cool down completely or it might be impossible to remove the card if any foreign material goes in the interface such as dirt or grime.

4.2 Wedgelock design

Since wedgelock design is the reference design, it is important to understand what the current state of the art is. As mentioned earlier, heat is conducted through dry contact from cards to cooling block. However, most of the heat transfers laterally through the card-cooling block interface, since there is no pressure on the bottom of the card. Also, since wedgelocks are hollowed, they are not a reliable means for heat transfer. As a result, most of the heat may transfer through one side only.

Figure 39 shows the heat transfer scheme for the wedgelock design:

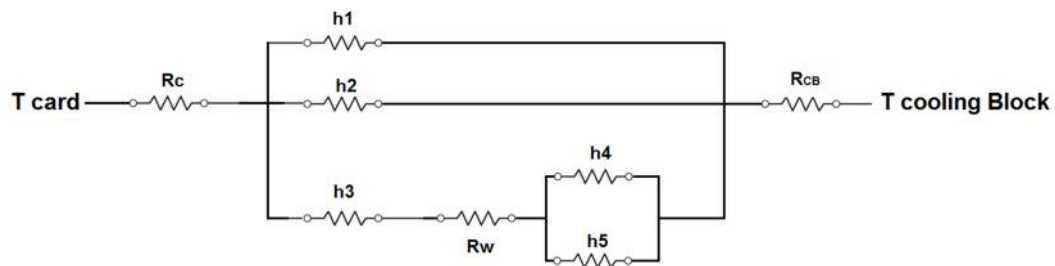


Figure 39: Heat transfer Scheme for Wedgelock Design

The total thermal resistance with respect to the thermal conductivity of the wedgelock can be found as follows:

$$R_{th} = \frac{h_1 A_1 h_2 A_2 R_{3-45-W}}{h_1 A_1 R_{3-45-W} h_2 A_2 + h_1 A_1 R_{3-45-W} h_1 A_1 h_2 A_2} + R_c + R_{CB}$$

.....(23)

Where R_{3-45-W} represents the equivalent thermal resistance of h_3 , R_w , h_4 , and h_5 .

Substituting our values and dimensions here we get:

$$R_{th} = 0.219 + \frac{8.82 k_w + 8.19}{(8.82 k_w + 8.19)0.05 + k_w}$$

.....(24)

In order to find the thermal resistance, it is required to find the thermal contact conductance coefficient (h_j) for each interface, where h_j is the inverse of the thermal resistance of the interface. Figure 40 below shows these interfaces:

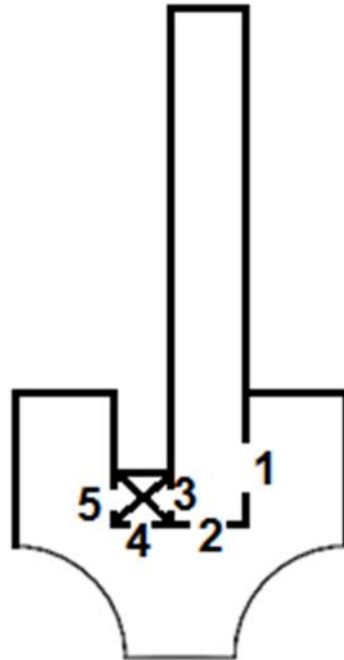


Figure 40: Thermal interfaces between Card, Cooling Block and Wedgelock

Yovanovich et al. [20, 69-71] provided a method to calculate the thermal contact conductance coefficient. This method proposes, as illustrated below, that the coefficient is the summation of two coefficients, one for gap and one for contact surfaces:

$$h_j = h_c + h_g \tag{ 25 }$$

Where h_c is:

$$h_c = 1.25 * k_s * \frac{m}{\sigma} \left(\frac{P}{H_c} \right)^{0.95} \tag{ 26 }$$

Where:

k_s is the harmonic mean thermal conductivity of the interface ,

$$k_s = 2 \times \frac{k_1 * k_2}{(k_1 + k_2)} \tag{ 27 }$$

σ is the effective RMS surface roughness of the contacting surfaces.

m is the effective mean absolute asperity slope of the interface[72]

Where $m_1 = m_2$

$$m_1 = m_2 = .125 * (\sigma * 10^6)^{0.402} \tag{ 28 }$$

H_c is the microhardness of AA6061 [20]

To find the thermal contact conductance coefficient for gap (h_g), the following equations can be used [20]:

$$Y = 1.53 * \sigma * \left(\frac{P}{H_c}\right)^{-0.097} \dots\dots\dots(29)$$

h_g can be found from:

$$h_g = \frac{k_g}{Y + M} \dots\dots\dots(30)$$

Where,

k_g is the thermal conductivity of air at operating temperature,

M is the gas parameter.

Figure 41 shows the thermal resistance with respect to the thermal conductivity.

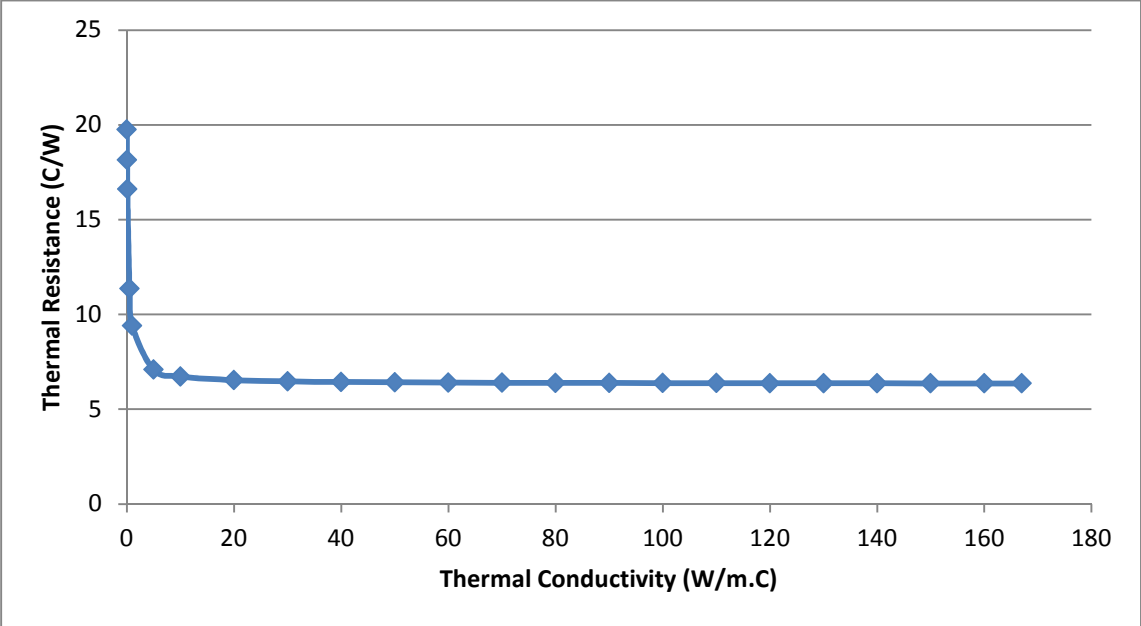


Figure 41: Thermal Conductivity Versus Thermal Resistance

Upon substituting the experimental value of the thermal resistance in equation (24), we notice that the thermal conductivity for the wedgelock cannot be more than $167 \text{ W/m}\cdot^{\circ}\text{C}$. In fact, it should be much less since the wedgelock is hollowed. However, there is no value for thermal conductivity that matches the experimental result of $0.35\pm 0.04 \text{ W/m}\cdot^{\circ}\text{C}$. It was found that the aforementioned equation can solve for the range of thermal resistances ($20.22 - 6.34$) $^{\circ}\text{C/W}$ only. Thus, the thermal conductivity cannot be estimated from the model above for our experiment. Further work will be done in the numerical analysis.

Another apparent issue is that since it is not possible to apply higher torque on the wedgelock than the manufacturer's recommended torque, it is not possible to optimize the pressure. Also, we can notice that the surface roughness affects the thermal resistance. The smoother the interface is, the lower the thermal resistance is. This can be achieved by either replacing the Aluminum with another material, or searching for a better finishing method for both surfaces. Either solution could be expensive and or difficult to do. Thus, we learn that if the wedgelock design cannot be optimized, finding alternatives was needed.

CHAPTER FIVE – NUMERICAL ANALYSIS

5.1 introduction

In this chapter, a numerical solution will be introduced to model and solve for the oil based ferrofluid design. The purpose of this analysis is to verify the experimental data, to optimize the ferrofluid thickness numerically, and to compare it with the analytical values, and finally to obtain temperature and flux distribution profile through the card and the cooling block. Thus, a complete analysis for the system will be obtained. The analysis of the system was performed using CD-adapco's STAR CCM+. Figure 42 shows the simulation process:

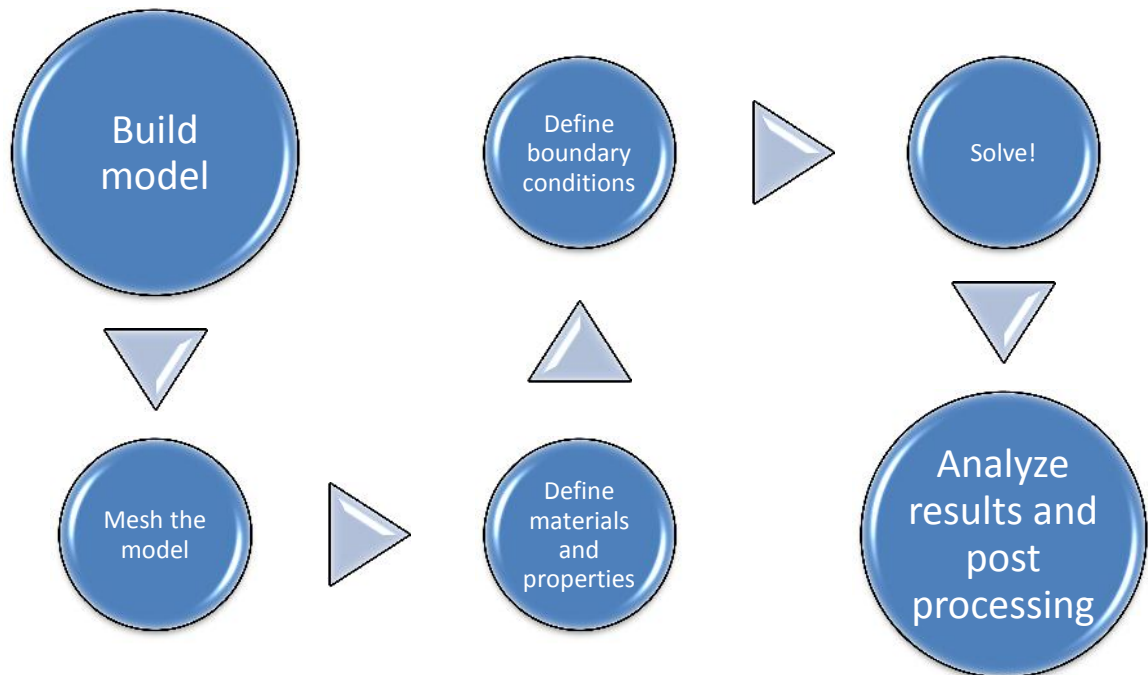


Figure 42: Simulation Process

5.2 Ferrofluid Design

The boundary conditions that were applied to the system in this analysis were based on data taken from experiments. For example, the cooling block temperature was measured using a thermocouple that is attached between the water channels of the cooling block. The data that was used in this analysis was taken at 143.83 Watts input power, since it was shown that at higher powers, the system is very stable.

Table 3 shows the boundary conditions that were considered, the heat flux was found by dividing the power over the area of the heater-card interface, which is 0.0025 m^2 :

Table 3: The Utilized Boundary Conditions

Cooling Block temperature K (C°)	Power (W)	Heat Flux (W/m ²)
294.1 (21.1)	143.83	55734.23

5.2.1 System Modeling and Meshing

Since the cooling block is symmetrical, only one card channel and two halves of the magnet channels were modeled. Two faces were generated: One for the card and one for the cooling block. The ferrofluid was modeled as interface material with thermal resistance based on variable film thickness. Heat flux of 55.73 kW/m^2 was applied on one side of the card to represent the heater in the experiment, while the rest of the card was at zero heat flux since it was insulated. Figure 43 below shows the model that was considered:

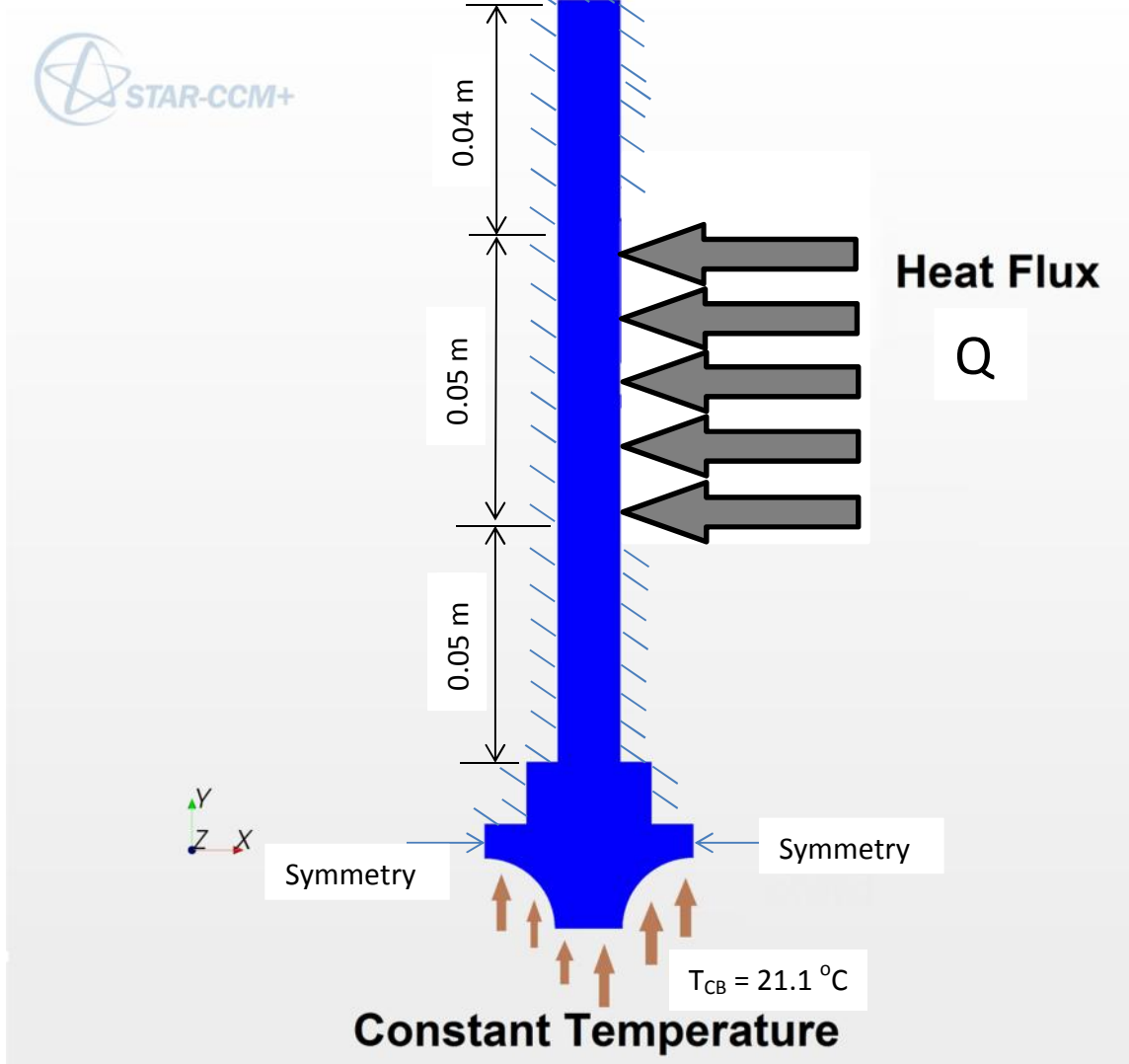


Figure 43: Model with Boundary Conditions

Since the ferrofluid layer is stationary, there is no need to solve the Navier-Stokes equation; therefore, energy equation was activated only.

5.2.2 Results, Mesh Study and Accuracy Check

In order to check the accuracy of the solution, three different mesh densities were examined. Figure 44 shows the scaled residuals of the three meshes:

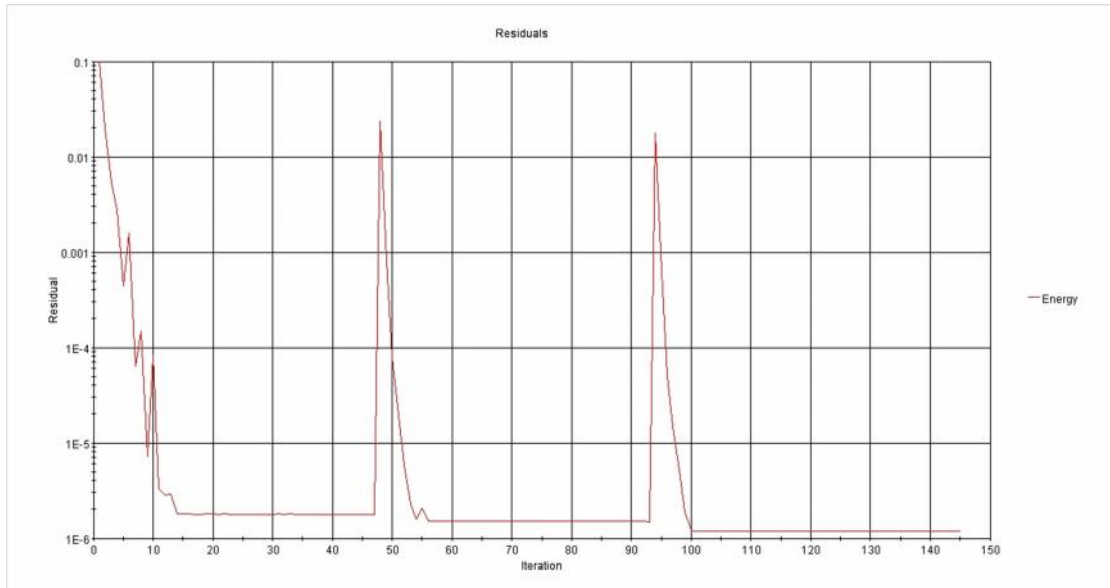


Figure 44: Scaled Residuals and Number of Iterations

The spikes in the figure above represent the points where the mesh was modified. Whenever the mesh was modified, the solver started all over again causing the appearance of these spikes, which disappeared quickly as the solution converged. Table 4 below shows comparison between the properties of the three meshes. The percentage difference column represents the percentage difference between numerical and experimental results and can be found from the following equation

$$\left| \frac{\text{numerical} - \text{experimental}}{\text{experimental}} \times 100\% \right|$$

The last column represents the difference between the input and output energies to the system. the closer the value to zero is, the more accurate the solution is.

Table 4: Mesh Study for ferrofluid design

Mesh	Cells	Interior Faces	Nodes	Card temperature at thermocouple Location (K)	Percentage difference	System total Heat Transfer Rate (W)
1	782062	2331410	1100489	339.2-316.6	5.4% -1.5 %	-1.4×10^{-02}
2	1112372	3319245	3319245	339.3-316.7	5.4% -1.5 %	2.3×10^{-03}
3	2043716	6105592	2928159	339.3-316.7	5.4% - 1.5%	-2.5×10^{-03}

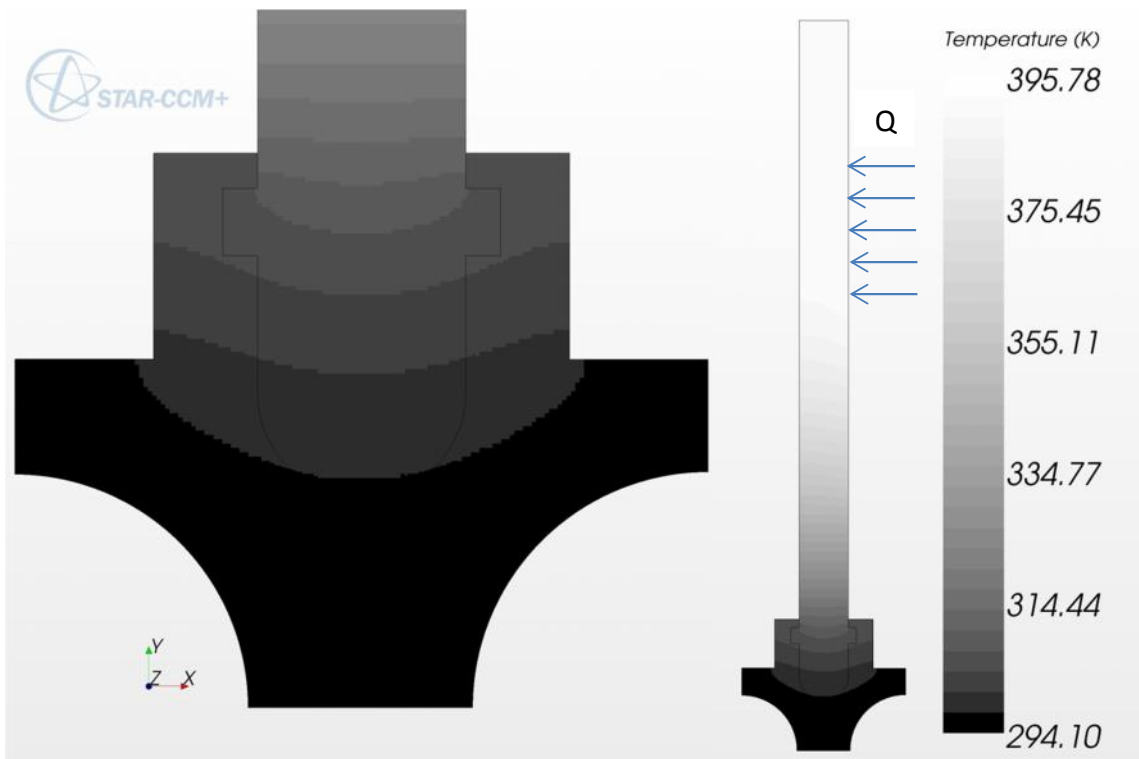


Figure 45: second Mesh Temperature Distribution for Ferrofluid design

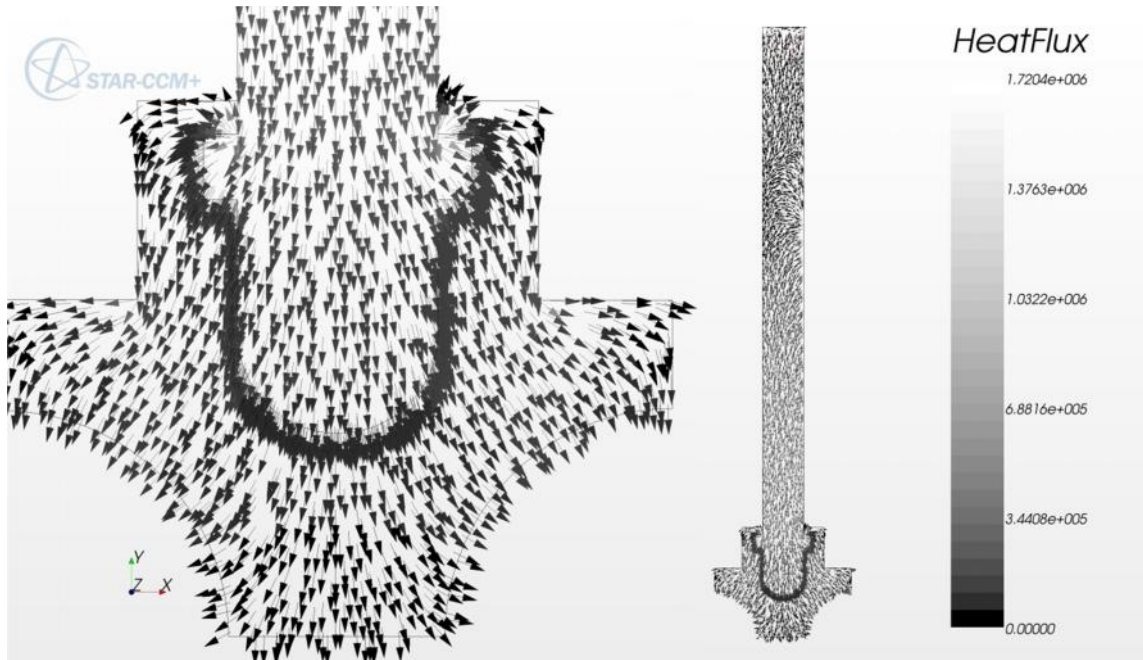


Figure 46: Second Mesh Heat Flux Distribution for ferrofluid design

Figure 47 below shows the mesh independency. The temperature of the card at the second point is more accurate than the first point due to mesh refinement. However, further mesh refinement has no effect on card temperature:

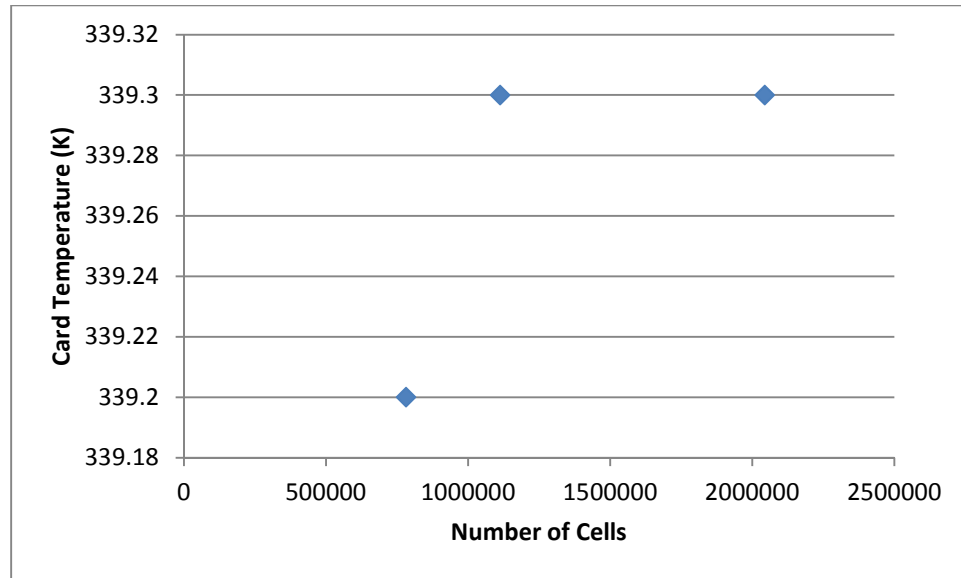


Figure 47: Mesh Study for ferrofluid design

From the previous results we conclude that the second mesh is the best one. Since the scaled residuals are very low (around 1×10^{-15}) and the summation of energies entering and exiting the system is close to zero, the solution is correct enough.

After choosing a suitable mesh model, it is possible to study the ferrofluid gap distance numerically by examining different gap spacings.

Table 5: Numerical Study for Gap Spacing (ferrofluid design)

Gap spacing (m)	Contact Resistance ($W/^{\circ}C .m^2$)	Card Temp (K)	Thermal Resistance ($^{\circ}K/W$)
2×10^{-03}	0.01265823	2550	15.6
1×10^{-03}	0.00632911	750	3.1
1×10^{-04}	0.00063291	375	0.3

1×10^{-5}	0.00006329	330	0.2
1×10^{-6}	0.00000633	320	0.1
1×10^{-7}	0.00000063	320	0.1
1×10^{-8}	0.00000006	320	0.1

Drawing the relation between the gap spacing and the thermal resistance results in figure 48. Figure 49 shows the same relation but for very small gap spacing.

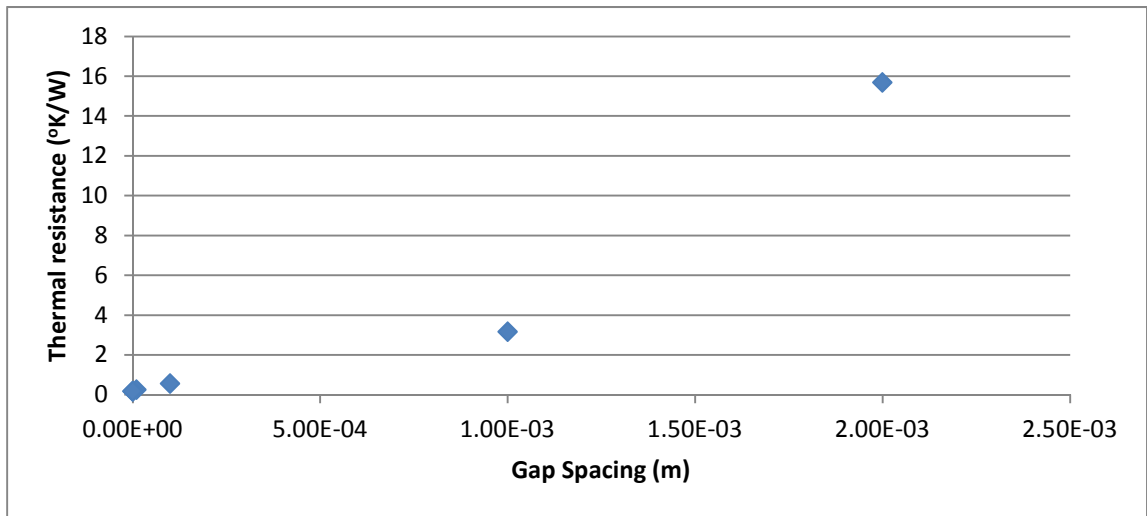


Figure 48: Numerical Relation between Gap Spacing and Thermal Resistance

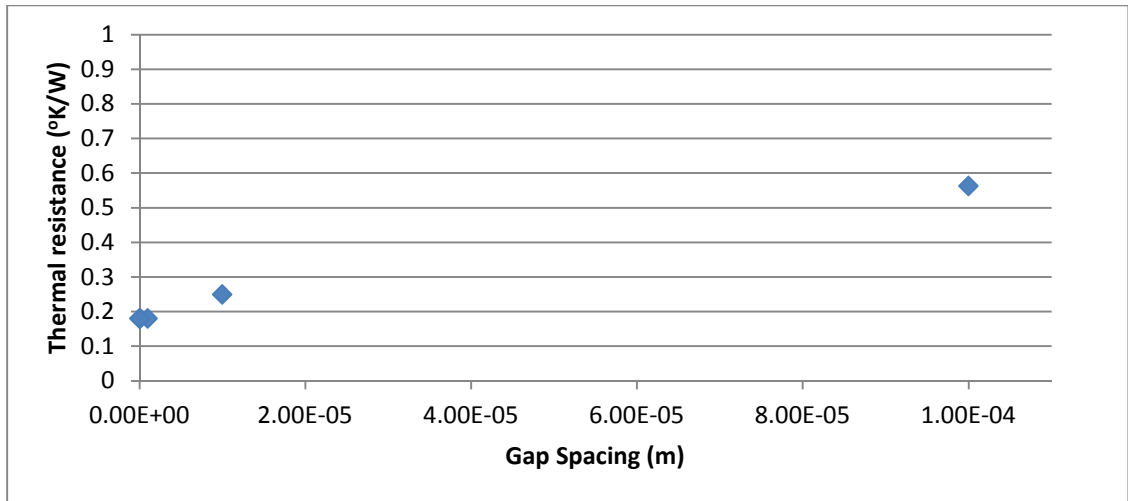


Figure 49: Numerical Relation between Gap Spacing and Thermal Resistance for very small gaps

From figures 48 and 49 we can understand the effect of gap spacing on the thermal resistance, the smaller the gap is, the higher the thermal conductivity is. Also, a gap of $0.1 \mu\text{m}$ would yield a thermal resistance of 0.18 K/W . However, the relationship is not expected to be linear due to the effect of the thermal expansion and the presence of the thermal interface material. Upon trial and error, it was found that a gap of $57.5 \mu\text{m}$ would result in a close thermal resistance to the experimental one. In general, to improve the current design, gaps of order of one micrometer should be considered.

5.3 Wedgelock Design

5.3.1 System Modeling and Meshing

The purpose of the numerical analysis of the wedgelock design is to understand the heat flux distribution and the temperature distribution, and to estimate the thermal conductivity of the wedgelock numerically.

The wedgelock design has five thermal interfaces, as mentioned before. Table 6 lists the conductance of these thermal interfaces:

Table 6: Conductance of the thermal Interfaces for wedgelock design

No.	Description	Value (kW/m ² . °C)
1	Card-Cooling Block – Right	15.24
2	Card-Cooling Block – Bottom	0.1
3	Card – Wedgelock	15.24
4	Wedgelock-Cooling Block - Bottom	0.1
5	Wedgelock-Cooling Block-Left	15.24

It is good to mention that the above interface conductance values were calculated using the Yovanovich method illustrated earlier in chapter four. However, it was found that the bottom interfaces, h_2 and h_4 , cannot be calculated using this method since the applied contact pressure is zero, which results in trivial solution. Thus, assuming a gap of 0.2 mm, based on the analysis of the ferrofluid design, it was found that the thermal resistance for these interfaces is 0.01 K.m²/W. The boundary conditions that have been considered are shown in table 7. Again, the heat flux was

found by dividing the power over the area of the heater-card interface, which is 0.0025 m²:

Table 7: Boundary Conditions for Wedgelock Design

Power input (W)	Heat Flux input (W/m ²)	Cooling block temperature °K (°C)
143.83	55734.23	292 (19)

The model to consider is shown in figure 50. Since the purpose of the analysis is to estimate the thermal conductivity for the wedgelock, an approximate model was built, which is a rectangular prism:

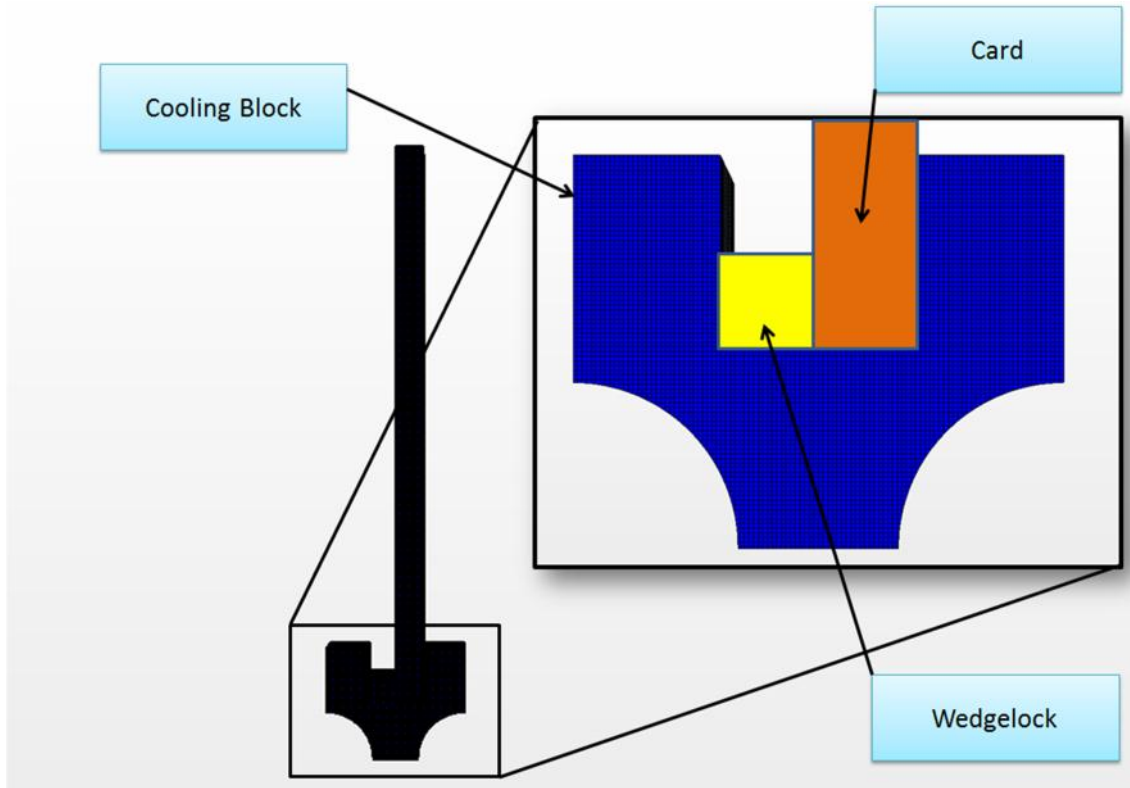


Figure 50: Numerical Model for Wedglock Design

The boundary conditions, i.e. heat generation and constant cooling block temperature, are located at the same places as the ferrofluid design.

5.3.2 Results, Mesh study and Accuracy Check

As in the ferrofluid design, three meshes will be considered in the mesh study. The scale residuals for the three meshes is shown in figure 51 below. The spikes represent the points where new analysis started all over again after mesh modification:

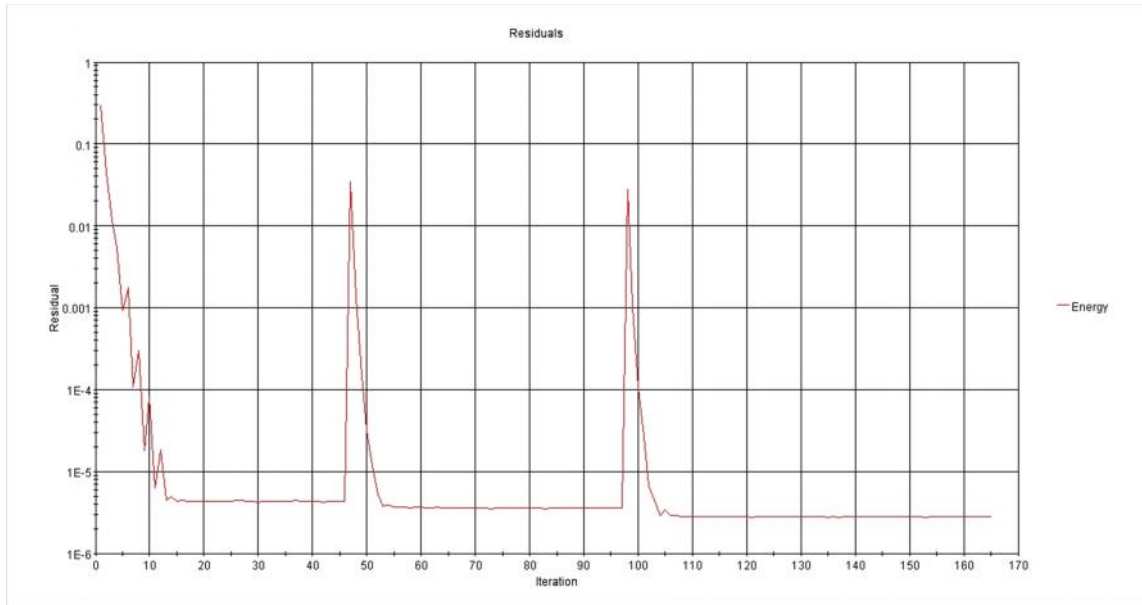


Figure 51: Scaled Residuals and Number of Iterations for wedgelock design

Table 8 shows comparison between the properties of the three meshes. The percentage difference is calculated in the same method as for the ferrofluid design:

Table 8: Mesh Comparison for wedgelock design

Mesh	Size			Card temperature at thermocouple Location (K)	Percentage difference From experimental results	System total Heat Transfer Rate (W)
	Cells	Interior Faces	Nodes			
1	114543	335773	194150	324.5	4.2%	0
2	198904	585836	299181	325	4.1%	0
3	336478	996225	496363	325.5	3.39%	0

From the results above, we notice that there is no huge difference between these three meshes. Thus, the first mesh will be considered.

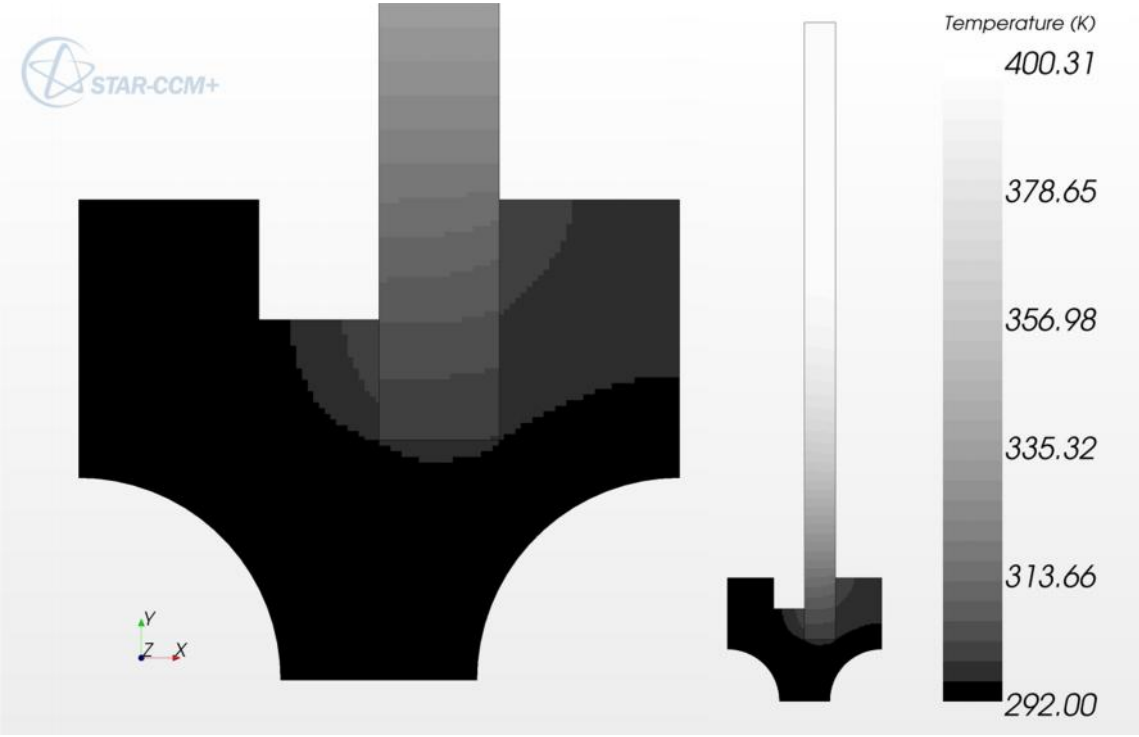


Figure 52: Temperature Distribution for the Wedgelock Design (First Mesh)

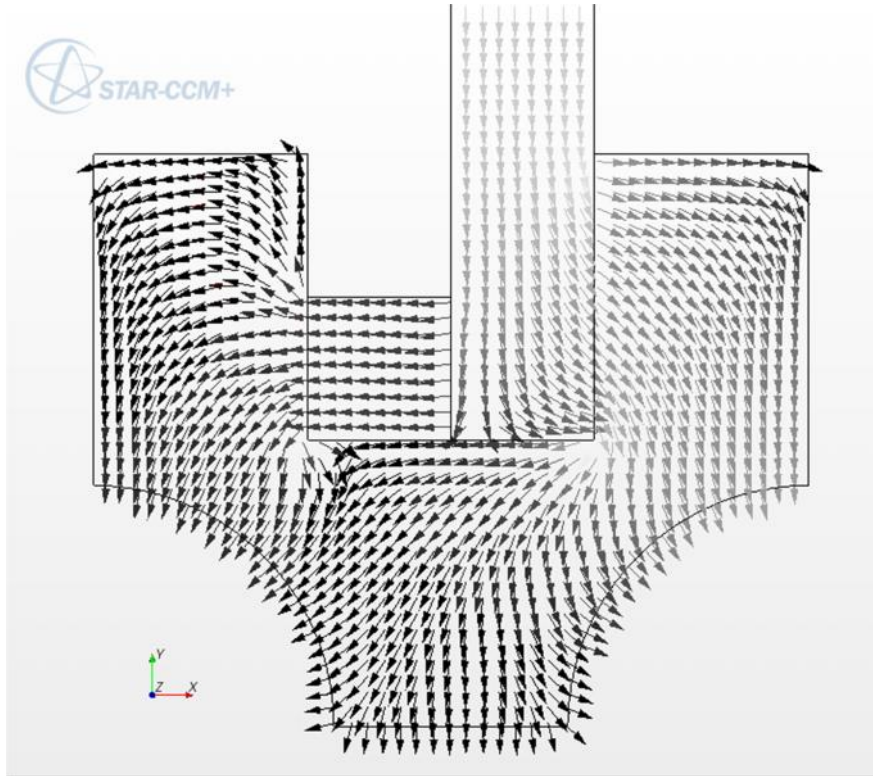


Figure 53: Heat flux Direction

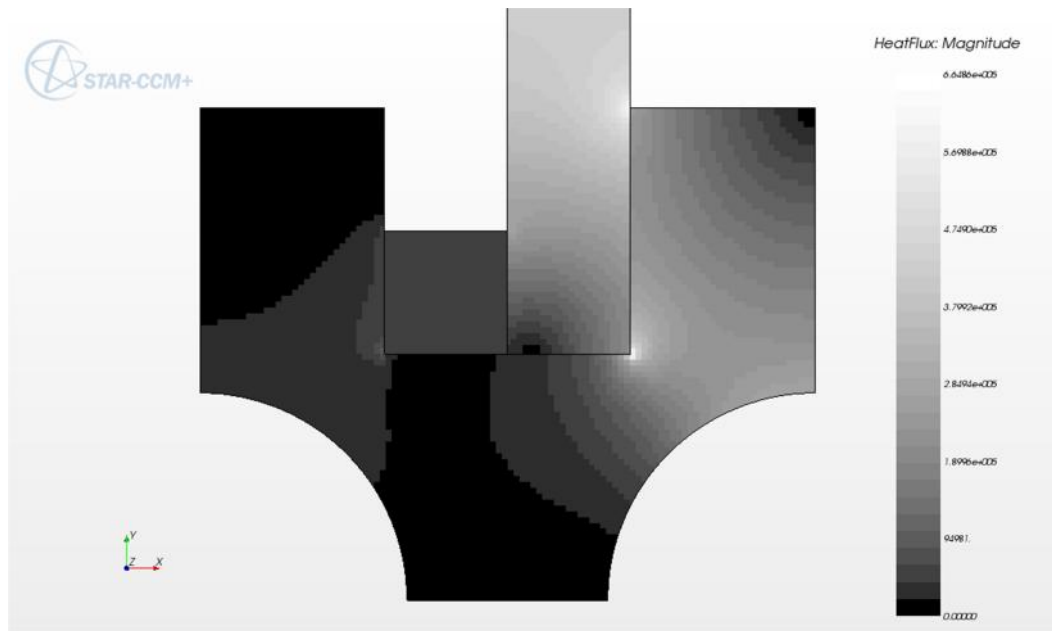


Figure 54: Heat flux Distribution

Figure 55 is the mesh study:

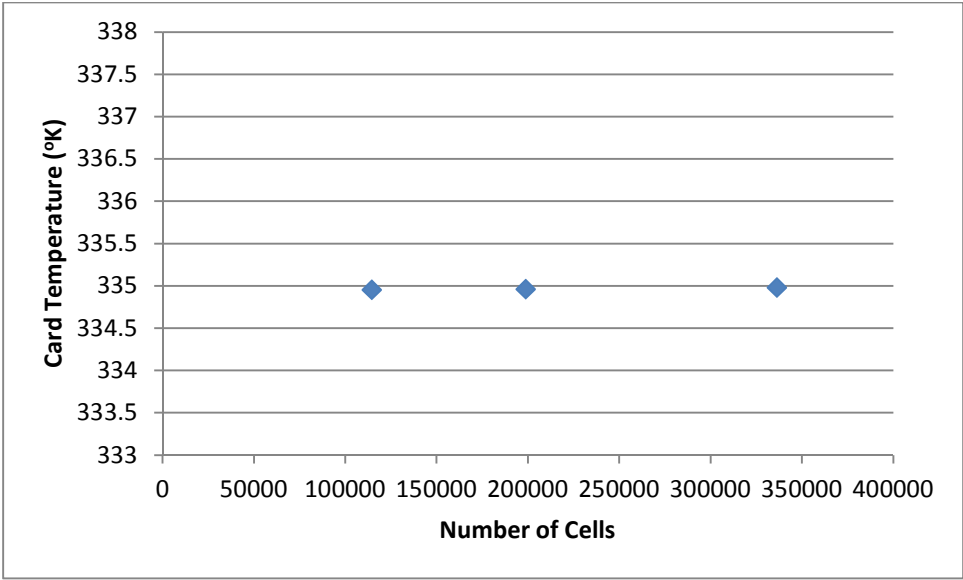


Figure 55: Mesh Study

As we can see, most of heat is transferred through the right of the card, although the thermal conductivity of the wedgelock was considered to be equal to that of the card and cooling block. This means that most of heat is dissipating at the interface between the card and the cooling block due to the low thermal resistance. Figure 56 is a study for the effect of the variation of the thermal conductivity of wedgelock on the thermal resistance:

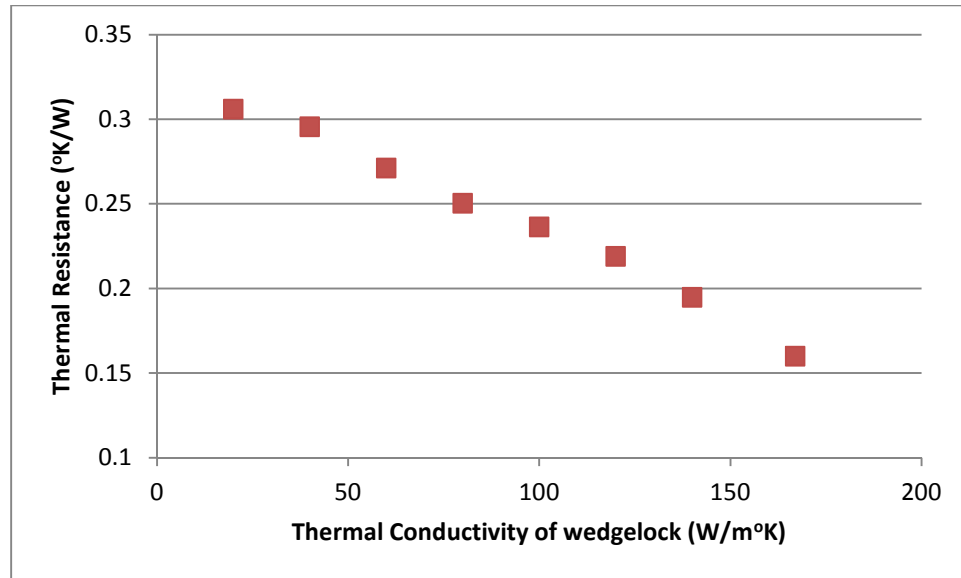


Figure 56: Thermal Conductivity of wedgelock Versus the Thermal Resistance

From figure 56 above we conclude that a wedgelock thermal resistance is slightly affected by the thermal conductivity of the wedgelock. However, as we have seen in the flux analysis, most of heat is transferred through the card-cooling block interface.

CHAPTER SIX – MAGNETIC ANALYSIS

As mentioned earlier in chapter four, in this chapter a study for optimizing magnets will be performed in order to estimate the lowest magnetic flux density required to hold the ferrofluid in place. In the following pages, a mathematical and numerical approach will be held to find these values.

6.1 Mathematical Analysis

In this analysis, one side of the cooling block and card will be studied since the other side is identical. One side includes ferrofluid that fills the gap between the aluminum wall and the card.

From the material safety and data sheet for the EFH1 ferrofluid provided by Ferrotech[49], the density of the ferrofluid is (1210 kg/m³). From the experiments, it was shown that one cubic centimeter of ferrofluid is enough for each side of the cooling block. By simple calculations, we find that the weight of this ferrofluid is:

$$m_f = 1210 \times 1 \times 10^{-6} \text{ kg}$$

$$m_f = 1.21 \times 10^{-3} \text{ kg}$$

.....(31)

Figure 57 shows mechanical analysis for the system:

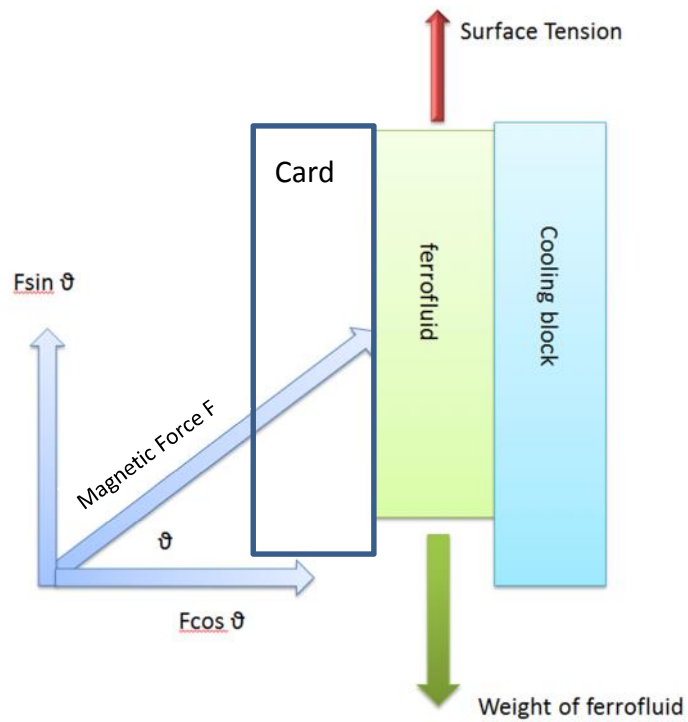


Figure 57: Forces Acting upon Ferrofluid

The ferrofluid is lifted up due to both the magnetic force component and the surface tension force.

Equation 32 below puts the description above into mathematical equation:

$$m_f \times g = F_{ST} + F \sin \theta$$

.....(32)

F_{ST} is the force of the surface tension. Franklin [73] used a tensiometer to measure the surface tension of the EFH1 oil based ferrofluid and found it to be **0.0258 N/m**.

Matsch [74] explain a method to calculate the magnetic force (F) with respect to the field density. The equation that Matsch had found is:

$$F = \frac{A B^2}{2 \mu_o} \dots\dots\dots(33)$$

Where,

A is the cross sectional area that the magnetic lines pass through.

B is the magnetic field intensity, measured in Tesla

μ_o is the permeability of vacuum, which is $(4\pi \times 10^{-7})$ h /m.

Reorganizing the aforementioned equations together, **B = 5.38×10^{-3} Tesla**, the least required magnetic field density to hold the ferrofluid in place.

Since

$$H = \frac{B}{\mu_o \mu_r} \dots\dots\dots(34)$$

Then H=4285.95 A/m

This means that at any field intensity larger than 4285.95 A/m the ferrofluid will be pulled upward against gravity. The H field varies depending on the magnets being used. The following data shows the effect of using different kinds of magnets of the same shape and dimensions mentioned earlier in chapter two but with different H field strengths:

Table 9: Results of Mathematical Analysis

H Field (A/m)	B Field (Tesla)	Magnetic Force (N)
8000	0.01	0.096
7000	0.0087	0.074
6000	0.0075	0.054
5000	0.0062	0.037
4285.95	0.0053	0.027
3000	0.0037	0.013
2000	0.0025	0.006
1000	0.0012	0.001
100	0.0001	1.51×10^{-5}
50	6.2×10^{-5}	3.7×10^{-6}

Table 9 was generated by picking different values for the magnetic force and finding the corresponding B field and H field from equations 29 and 30. Figures 58, 59 and 60 are the graphs for these results:

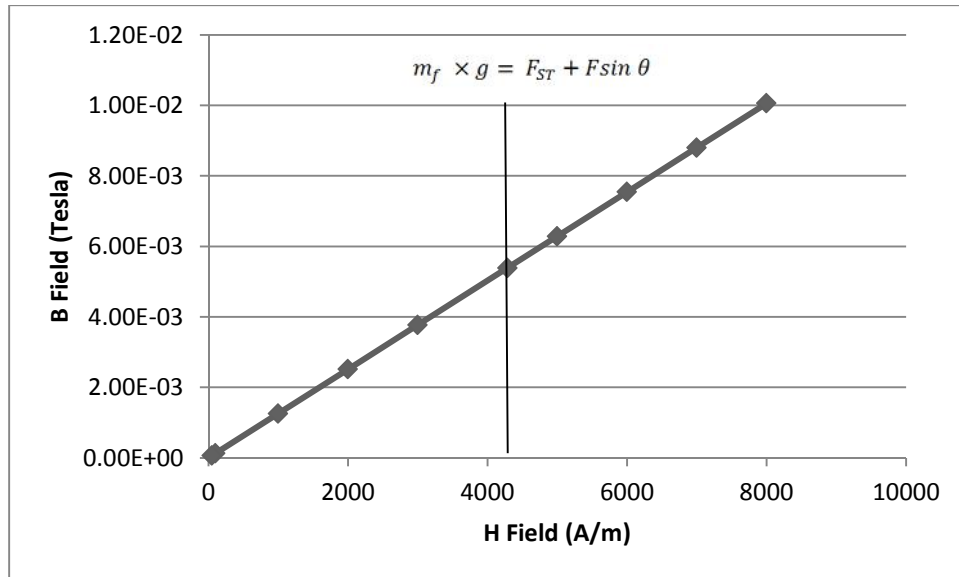


Figure 58: H-Field versus B-Field. Any Value to the right of the vertical line can pull the ferrofluid upward

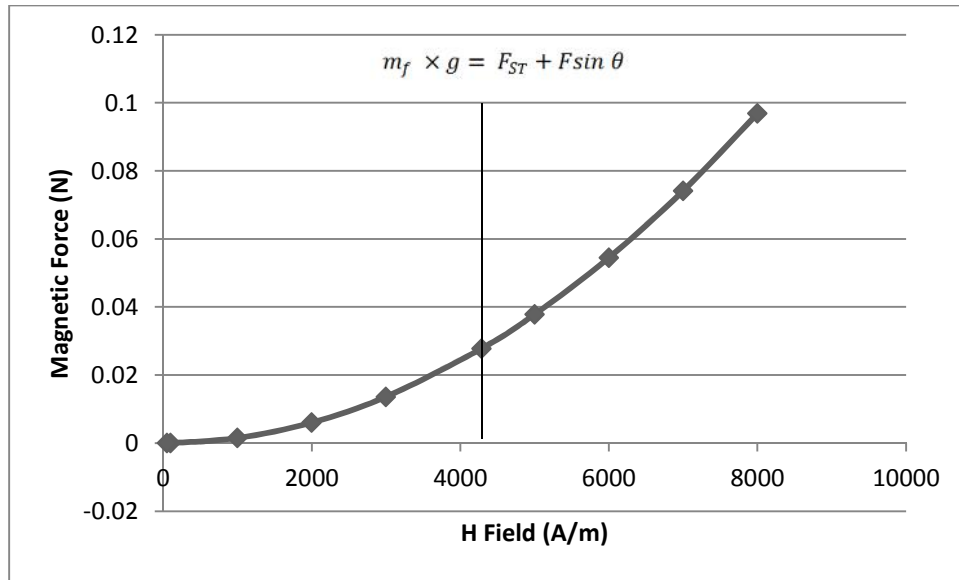


Figure 59: H-Field versus the Magnetic Force. Again, the values to the right of the vertical line can pull the ferrofluid upward.

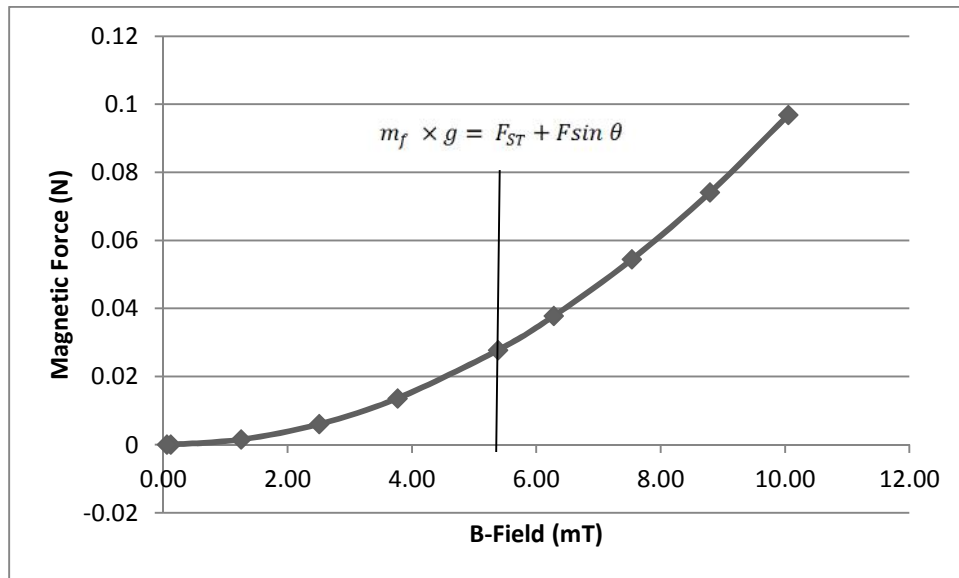


Figure 60: B-Field versus Magnetic Force. The values to the right of the vertical line can pull the ferrofluid upward.

6.2 Numerical Analysis

The numerical analysis can be useful to show the magnetic density distribution, to show the direction of the magnetic field, and to calculate the coercive force (H_c) property for the magnet necessary to hold the ferrofluid in place. The magnets that had been used in the experimental analysis were purchased from K&J Magnetics. The seller lists on its website that the coercive force for N52 neodymium magnet is larger than 11.2 KOe or 900 A/m. Thus, it is unclear what value the coercive force should be in order to hold the ferrofluid; however, the numerical analysis might provide estimation for this magnetic property.

In this thesis, Finite Element Method Magnetics (FEMM) was used to carry out the analysis because of its ability of solving magnetics problems. Figure 61 shows the main screen for FEMM:

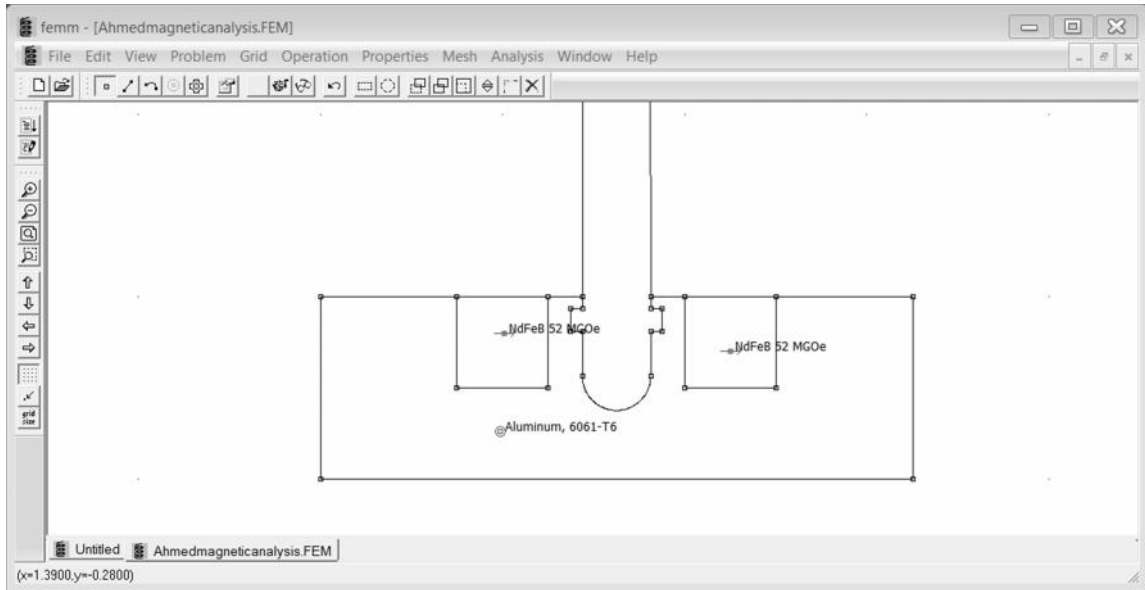


Figure 61: Finite Elements Method Magnetics (FEMM) Main Screen

6.2.1 Modeling

In order to model the device, two rows of magnets are required to model so that it matches the experimental setup. The following model was generated:

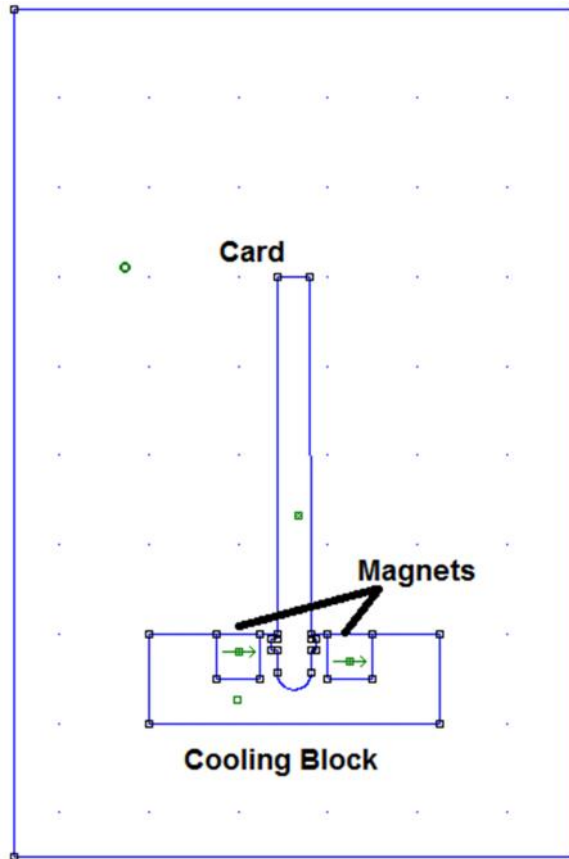


Figure 62: FEMM Model for Ferrofluid Design

6.2.2 Results and Post Processing

After meshing and solving the system, the results for different coercive forces were collected and shown below in table 10 starting with the minimum coercive force anticipated by the supplier:

Table 10: Results of numerical analysis

Trial No.	Coercive Force (A/m)	Magnetic Flux Density at Ferrofluid Location (T)	Percentage difference from analytical solution %
1	900	1.7×10^{-4}	96.8
2	1200	2.4×10^{-4}	95.5
3	3000	5.9×10^{-4}	89.0
4	10000	2.0×10^{-3}	62.8
5	11000	2.2×10^{-3}	59.1
6	15000	3.0×10^{-3}	44.2
7	19000	3.7×10^{-3}	31.2
8	24000	4.7×10^{-3}	12.6
9	25000	5.0×10^{-3}	7.0
10	26000	5.31×10^{-3}	1.3
11	26500	5.44×10^{-3}	1.1
12	27000	5.6×10^{-3}	4.0
13	30000	6.0×10^{-3}	11.5

We can notice that a coercive force of 900 A/m would not produce the desired field density. Upon trying different coercivities, trial eleven has the lowest error percentage and the best match to the analytical values. We will pick trial eleven as the numerical value for the least coercive force required to produce a B-field strong

enough to equalize the surface tension and weight of ferrofluid. The relation between the coercive force and the flux density is shown below in figure 63:

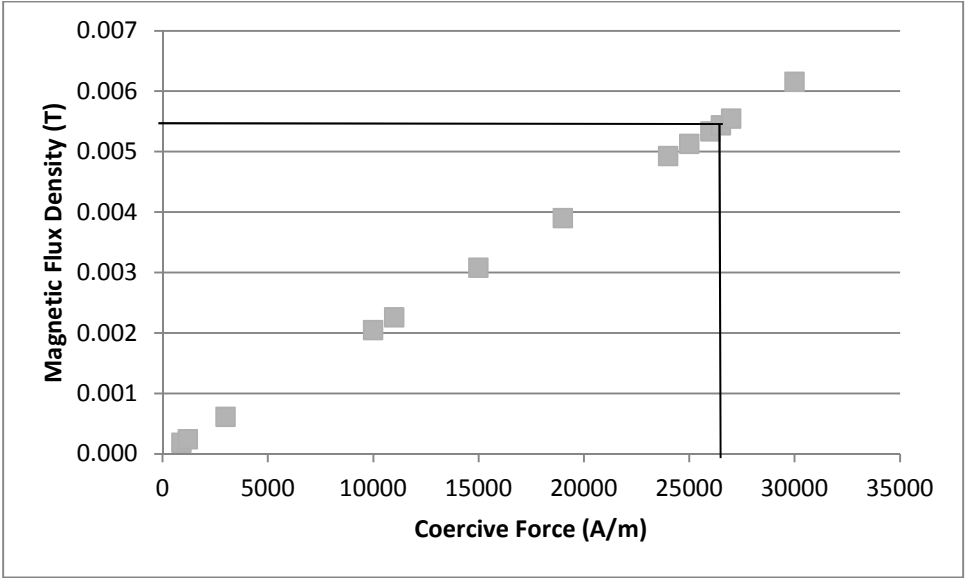


Figure 63: Relation between Coercive force and magnetic flux density

From figure 63 above, the relation looks linear and proportional between the coercive force and the magnetic flux density as was expected. The intersection of the vertical and horizontal lines with coordinates represents the least coercive force and its B field required to equalize the ferrofluid forces. The coercive force is important since it is one of the properties of the magnets and represents how strong the magnets are.

Figures 64 and 65 shows the magnetic flux density distribution and direction for a coercive force of 26500 A/m

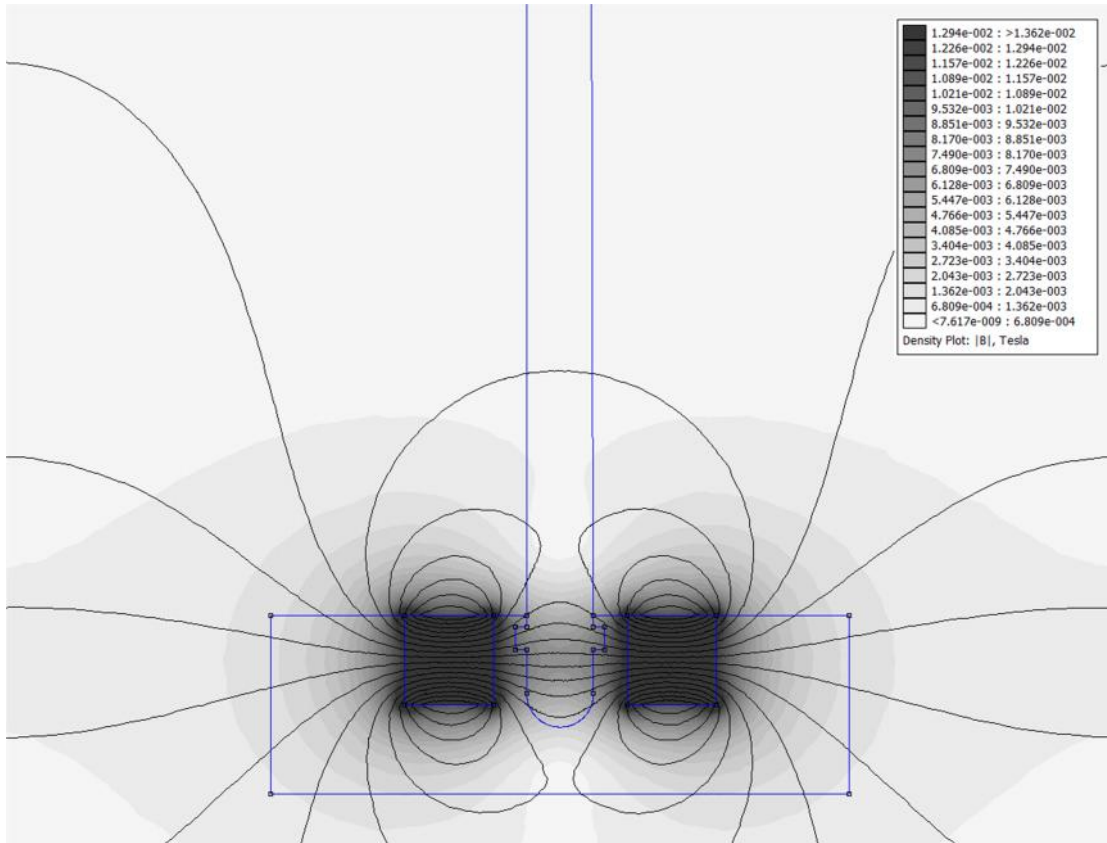


Figure 64: Magnetic Flux Density Distribution

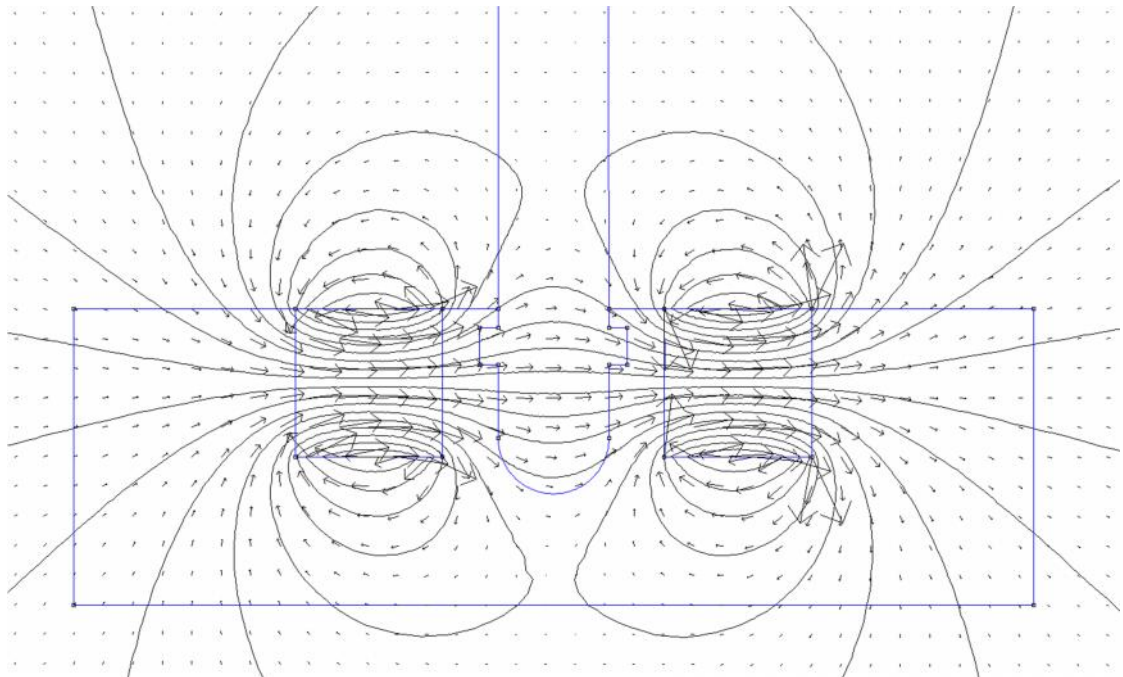


Figure 65: Vector representation for the Flux Density, showing its direction

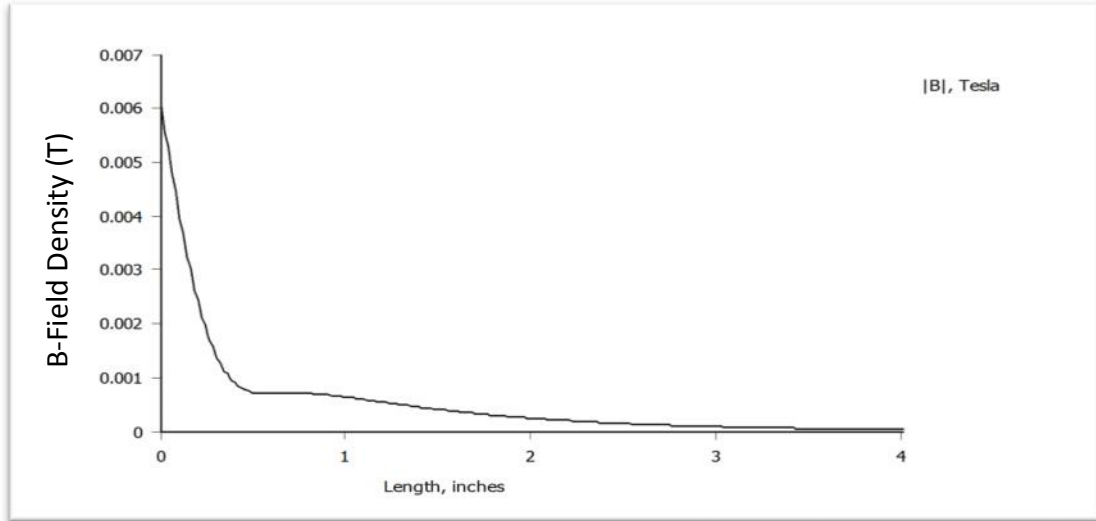


Figure 66: B-Field density drop along the height of the card

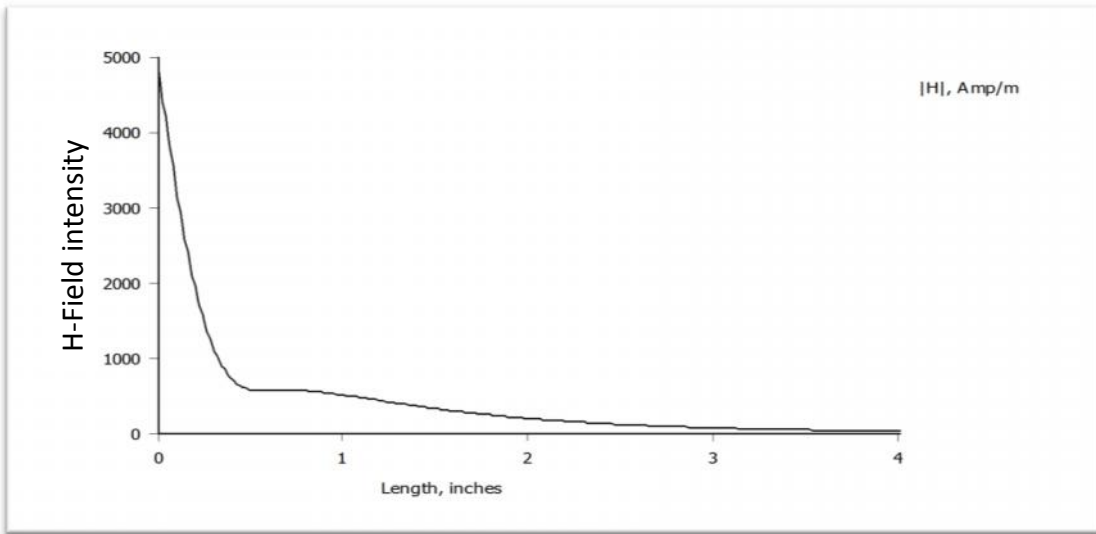


Figure 67: H-Field intensity drop along the height of the card

From figure 64 and 65, it is very clear that the magnetic effect drops as soon as it leaves the cooling block. Figures 66 and 67 show this drop along the length of the card. This quick drop in field density to less than 0.001 T at one inch from the cold block is preferred since it can eliminate the interaction with the electronic parts on the card.

CHAPTER SEVEN – CONCLUSION AND CLOSURE

The purpose of this thesis was mainly to optimize the ferrofluid design that was presented earlier by the University of Missouri RevCon team. From the experimental, analytical, and numerical results that were obtained, the ferrofluid design can be recommended for future investigation and research. Oil based ferrofluid showed that it can handle many operating hours without evaporation. Also, the thermal resistance of the new design is less than the thermal resistance for the wedgelock design, which suffers from many deficiencies that affect its properties. In addition, a suggested method for wiping the card was explained. This may not seem to be very efficient; however, precise manufacturing for the wiping assembly could improve its function considerably. Thus, improving the wiping assembly and providing alternatives may be left for future work. Also, it might be beneficial to explore other versions of ferrofluids.

As mentioned before, ferrofluid properties may differ greatly according to the base fluid. As a result, investigating another ferrofluid with high thermal conductivity and evaporation proof can be of interest.

Another point that is worthy to mention is that this design is meant for high end military applications. This means that it is subject to shock, vibration, and flipping. Consequently, tests for these criteria are very important in order to estimate the behavior of the design in such tough conditions.

A magnetic analysis was performed, too. The purpose was to estimate the required magnetic force to lift the ferrofluid and hold it in place. Also, the magnetic flux

density and intensity were calculated and a mathematical relation between them was estimated.

Finally, the use of an entirely aluminum card is meant for making calculations easier. Since the interface design worked for the aluminum card, this means that it can work for any printed circuit boards found in real applications, whether it had a copper rail attached to it or not.

APPENDIX-A-MANUFACTURING PROCESS FOR THE NEW CARD

The manufacturing process started by taking random piece of Aluminum Alloy 6061 of two inches thickness and cutting it into the following dimensions: 6 ×5.5 ×0.5 inches.

We started by marking a horizontal line at 4.5 inches as in figure 68:

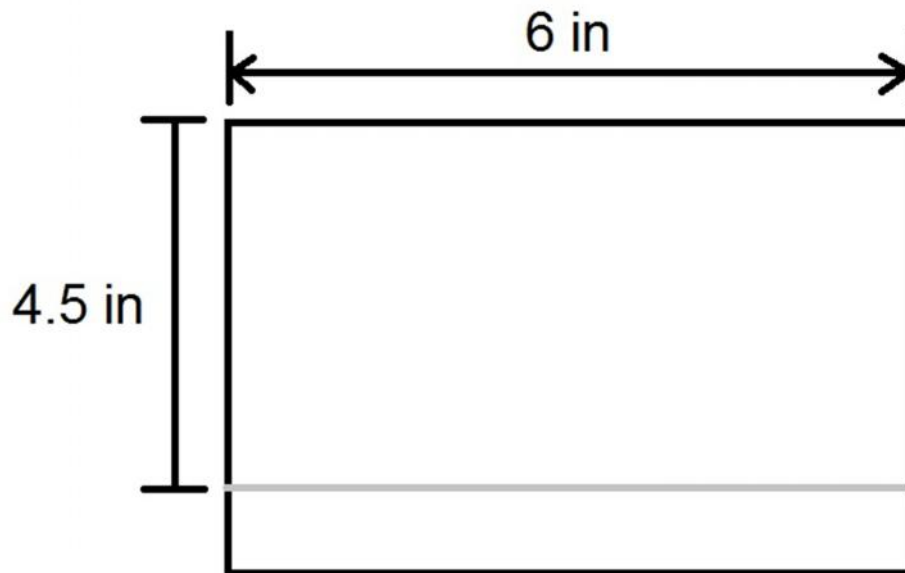


Figure 68: Dimensions for New Card

Next, using the plain milling cutter tool (figure 69), the area 6 ×4.5 inches would be machined from both sides the amount of 0.126 inches. The resulting shape is shown in figure 70:



Figure 69: Plain milling cutter tool

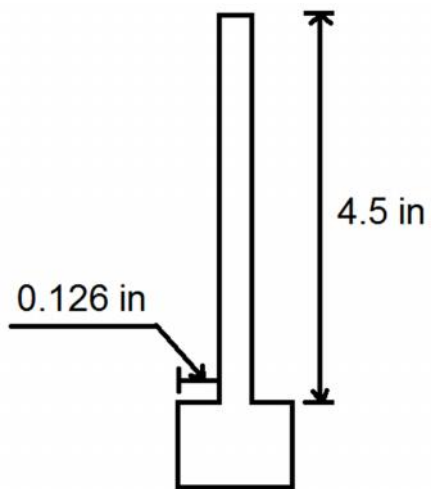


Figure 70: Card After first Horizontal Milling

After that, using the same cutter, we cut 0.063 inches from both sides, as shown in figure 71:

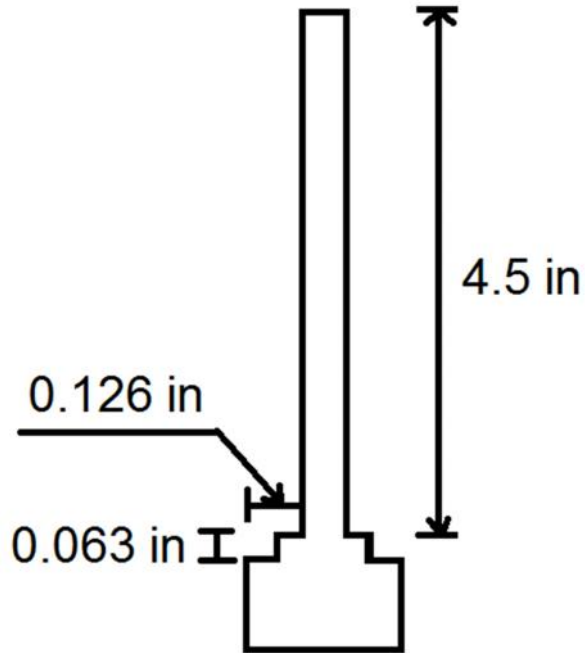


Figure 71: Card After Second Horizontal Milling

Now leaving 0.125 inches from both sides, at the same depth of 0.063 inches the cutting process continued until the edge of the card. The resulting shape is shown in figure 71.

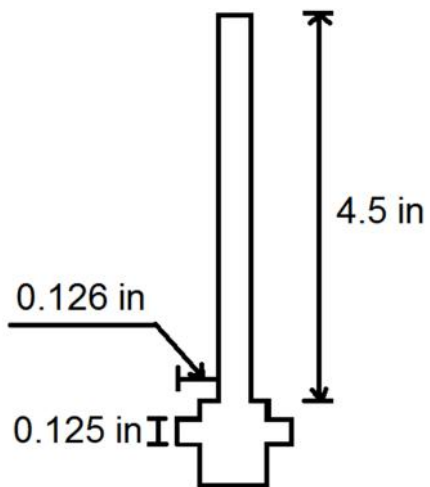


Figure 72: Card After Third Horizontal Milling

Now using the corner rounding tool shown in figure 73, the round edges had been machined:



Figure 73: Corner Rounding Tool

Thus, the final shape would look like in figure 74:

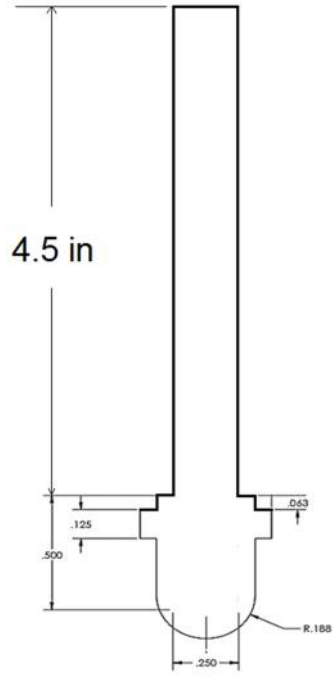


Figure 74: Final Shape

BIBLIOGRAPHY

1. Howard, C.E. *Avionics and military electronics thermal management challenges are sparking innovative solutions to keep these systems cool - Avionics Intelligence*. Avionics Intelligence 2010 2010/11/04/2013/03/26/17:17:23.
2. Curtiss-Wright. *Acra Proven in Low Earth Orbit*. 2011 [cited 2013 March 28].
3. Curtiss-Wright, *KAM-500 chassis with 9 user-slots and MB2 option*, KAM_CHS_09U_E_MB2.jpg, Editor., Curtiss-Wright
4. Harding, P., *ISS performs hardware and software upgrades to support inaugural Dragon visit*. 2012, NASASpaceflight.
5. 3M, *Technical Bulletin: Characteristics of Thermal Interface Material*, 3M, Editor. January 2001.
6. Prasher, R., *Thermal Interface Materials: Historical Perspective, Status, and Future Directions*. Proceedings of the IEEE, 2006. **94**(8): p. 1571-1586.
7. Fletcher, L.S., *A review of thermal enhancement techniques for electronic systems*. Components, Hybrids, and Manufacturing Technology, IEEE Transactions on, 1990. **13**(4): p. 1012-1021.
8. ebruary, I., *Materials for advanced packaging [electronic resource]*. 2009, New York: Springer.
9. AAVIDThermalloy. *Thermal Greases*.
10. EVGA. *EVGA Frostbite: Super cool*. 2011.
11. AMD, *Thermal Interface Material Comparison: Thermal Pads vs. Thermal Grease*. April 2004, Advanced Micro Devices.
12. 3M, *3M™ Thermally Conductive Adhesive Transfer Tapes*. April, 2008, Electronics Markets Materials Division at 3M Electronics.
13. Corning, D., *Information about Dow Corning Brand Thermal Interface Pads and Films*, D.C.E. Solutions, Editor. 2003: United States of America.
14. Landauer, R. *Electrical conductivity in inhomogeneous media*. in *AIP Conference Proceedings*. 1978.
15. Every, A., et al., *The effect of particle size on the thermal conductivity of ZnS/diamond composites*. Acta metallurgica et materialia, 1992. **40**(1): p. 123-129.
16. Devpura, A., P.E. Phelan, and R. Prasher. *Percolation theory applied to the analysis of thermal interface materials in flip-chip technology*. in *Thermal and Thermomechanical Phenomena in Electronic Systems, 2000. ITherm 2000. The Seventh Intersociety Conference on*. 2000. IEEE.
17. Yovanovich, M.M. and E.E. Marotta, *Thermal spreading and contact resistances*. Heat Transfer Handbook, 2003. **1**: p. 261-394.
18. Madhusudana, C.V., *Thermal contact conductance*. 1995: Springer.
19. LienhardIV, J.H. and J.H. LienhardV, *A Heat Transfer Textbook*. Third Edition ed. 2008, Cambridge, Massachusetts: Phlogiston Press.

20. Yovanovich, M. *New contact and gap correlations for conforming rough surfaces*. in *AIAA 16th Thermophysics Conference*. 1981.
21. Stix, G., *Little Big Science*. Scientific American.com, September 16, 2001.
22. Feynman, R.P., *Plenty of Room at the Bottom*. 1959, California Institute of Technology: Pasadena, California.
23. Taniguchi, N., *On the Basic Concept of 'Nano-Technology'*. Bulletin of the Japan Society of Precision Engineering, 1974. **II**: p. 18-23.
24. Drexler, E., *Engines of Creation: The Coming Era of Nanotechnology*. 1987: Anchor.
25. Regis, E., *The Incredible Shrinking Man*, in *Wired.com*. 2004. p. 1-4.
26. Giles, J., *Nanotech takes small step towards burying 'grey goo'*. Nature, 2004: p. 429 (6992): 591.
27. Nobelprize.org, *The 1986 Nobel Prize in Physics: Ernst Ruska, Gerd Binnig, Heinrich Rohrer*, in *The Nobel Prize in Physics 1986*. 1986.
28. Binnig, G. and H. Rohrer, *Scanning tunneling microscopy*. IBM Journal of Research and Development, 1986: p. 30: 4.
29. Timofeeva, E.V., et al., *Nanofluids for Heat Transfer: An Engineering Approach*, in *Nanoscale Research Letters*. 2010, Argonne National Laboratory: Argonne, IL, 60439, USA.
30. Timofeeva, E.V., et al., *Base fluid and temperature effects on the heat transfer characteristics*. JOURNAL OF APPLIED PHYSICS, 2011(014914): p. 109.
31. Lee, S., et al., *Measuring thermal conductivity of fluids containing oxide nanoparticles*. Journal Name: Journal of Heat Transfer; Journal Volume: 121; Journal Issue: 2; Other Information: PBD: May 1999, 1999: p. 280-289.
32. Touloukian, Y., *Thermal Properties Of Matter: Thermal Conductivity of Solids*. 1970, Plenum, New York, NY.
33. Choi, S.U.S. and J.A. Eastman. *Enhancing thermal conductivity of fluids with nanoparticles*.
34. Eastman, J.A., et al., *Anomalously increased effective thermal conductivities of ethylene glycol-based nanofluids containing copper nanoparticles*. Applied Physics Letters, 2001. **78**(6): p. 718-720.
35. Hong, K.S., T.-K. Hong, and H.-S. Yang, *Thermal conductivity of Fe nanofluids depending on the cluster size of nanoparticles*. Applied Physics Letters, 2006. **88**(3).
36. Kumar, D.H., et al., *Model for heat conduction in nanofluids*. Physical Review Letters, 2004. **93**(14).
37. Xuan, Y. and Q. Li, *Heat transfer enhancement of nanofluids*. International Journal of Heat and Fluid Flow, 2000. **21**(1): p. 58-64.
38. Gavili, A., M. Lajvardi, and J. Sabbaghzadeh, *The Effect of Magnetic Field Gradient on Ferrofluids Heat Transfer in a Two-Dimensional Enclosure*. Journal of Computational and Theoretical Nanoscience, 2010. **7**(8): p. 1425-1435.
39. Nagasaka, Y. and A. Nagashima, *Precise Measurement of the Thermal Conductivity of Liquids(2 nd Report, An Absolute Measurement of the Thermal*

- Conductivity of Electrically Conducting Liquids by the Transient Hot-Wire Method*). TRANS. JAPAN SOC. MECH. ENG., 1981. **47**(419): p. 1323-1331.
40. Xue, Q.-Z., *Model for effective thermal conductivity of nanofluids*. Physics Letters A, 2003. **307**(5-6): p. 313-317.
 41. Maxwell, J.C., *A treatise on electricity and magnetism*. Vol. 1. 1881: Clarendon press.
 42. Hamilton, R.L. and O.K. Crosser, *Thermal Conductivity of Heterogeneous Two-Component Systems*. Industrial & Engineering Chemistry Fundamentals, 1962. **1**(3): p. 187-191.
 43. Jeffrey, D.J., *Conduction through a random suspension of spheres*. Proceedings of the Royal Society of London. A. Mathematical and Physical Sciences, 1973. **335**(1602): p. 355-367.
 44. Davis, R., *The effective thermal conductivity of a composite material with spherical inclusions*. International Journal of Thermophysics, 1986. **7**(3): p. 609-620.
 45. Lu, S.Y. and H.C. Lin, *Effective conductivity of composites containing aligned spheroidal inclusions of finite conductivity*. Journal of Applied physics, 1996. **79**(9): p. 6761-6769.
 46. Yu, W. and S. Choi, *The role of interfacial layers in the enhanced thermal conductivity of nanofluids: a renovated Maxwell model*. Journal of Nanoparticle Research, 2003. **5**(1-2): p. 167-171.
 47. Jang, S.P. and S.U. Choi, *Role of Brownian motion in the enhanced thermal conductivity of nanofluids*. Applied physics letters, 2004. **84**(21): p. 4316-4318.
 48. Corporation, F.U., *MATERIAL SAFETY DATA SHEET FOR Water Based Ferrofluid*, in *EMG700*. February 3, 2009.
 49. Corporation, F.U., *MATERIAL SAFETY DATA SHEET - Oil based Ferrofluid*, in *EFH Series*. March 18, 2009.
 50. Jolivet, J.P.M., R.; Fruchart, J. M., *Synthesis and physicochemical study on nonsurfactant magnetic colloids in aqueous medium*. Nouv. J. Chim., 1983. **7**(5).
 51. Yiping, L., et al., *Co-Pt-B particles prepared by chemical reduction*. Magnetics, IEEE Transactions on, 1993. **29**(6).
 52. Kobayashi, Y., et al., *Preparation and Properties of Silica-Coated Cobalt Nanoparticles*. The Journal of Physical Chemistry B, 2003. **107**(30): p. 7420-7425.
 53. Pileni, M.P., *Nanosized Particles Made in Colloidal Assemblies*. Langmuir, 1997. **13**(13): p. 3266-3276.
 54. Petit, C. and M.P. Pileni, *Nanosize cobalt boride particles: Control of the size and properties*. Journal of Magnetism and Magnetic Materials, 1997. **166**(1-2): p. 82-90.
 55. Duxin, N., et al., *Nanosized Fe-Cu-B Alloys and Composites Synthesized in Diphasic Systems*. The Journal of Physical Chemistry B, 1997. **101**(44): p. 8907-8913.

56. Lisiecki, I. and M.P. Pileni, *Synthesis of Well-Defined and Low Size Distribution Cobalt Nanocrystals: The Limited Influence of Reverse Micelles*. Langmuir, 2003. **19**(22): p. 9486-9489.
57. Ely, T.O., et al., *Synthesis of Nickel Nanoparticles. Influence of Aggregation Induced by Modification of Poly(vinylpyrrolidone) Chain Length on Their Magnetic Properties*. Chemistry of Materials, 1999. **11**(3): p. 526-529.
58. Zitoun, D., et al., *Magnetic enhancement in nanoscale CoRh particles*. Phys Rev Lett, 2002. **89**(3): p. 037203.
59. Dumestre, F., et al., *Superlattices of Iron Nanocubes Synthesized from Fe[N(SiMe₃)₂]₂*. Science, 2004. **303**(5659): p. 821-823.
60. Salgueiriño-Maceira, V., L.M. Liz-Marzán, and M. Farle, *Water-Based Ferrofluids from FePt_{1-x} Nanoparticles Synthesized in Organic Media*. Langmuir, 2004. **20**(16): p. 6946-6950.
61. Sun, S., et al., *Monodisperse FePt Nanoparticles and Ferromagnetic FePt Nanocrystal Superlattices*. Science, 2000. **287**(5460): p. 1989-1992.
62. Euliss, L.E., et al., *Cooperative Assembly of Magnetic Nanoparticles and Block Copolypeptides in Aqueous Media*. Nano Letters, 2003. **3**(11): p. 1489-1493.
63. Massart, R., *Preparation of aqueous magnetic liquids in alkaline and acidic media*. Magnetics, IEEE Transactions on, 1981. **17**(2): p. 1247-1248.
64. Correa-Duarte, M.A., et al., *Control of Packing Order of Self-Assembled Monolayers of Magnetite Nanoparticles with and without SiO₂ Coating by Microwave Irradiation*. Langmuir, 1998. **14**(22): p. 6430-6435.
65. Wiese-Fales, J. *Team's proposal earns 'Most Creative' prize at RevCon Challenge*. 2012 [cited 2013 March 28].
66. OmegaElectronics, *Revised Thermocouple Reference Tables*.
67. *Permanent magnet motor technology: design and applications*. Vol. 113. 2002, New York: Marcel Dekker.
68. Incropera, F.P., *Introduction to heat transfer*. 2007, Hoboken, N.J: Wiley.
69. Cooper, M.G., B.B. Mikic, and M.M. Yovanovich, *Thermal contact conductance*. International Journal of Heat and Mass Transfer, 1969. **12**(3): p. 279-300.
70. Antonetti, V.W. and M. Yovanovich, *Thermal contact resistance in microelectronic equipment[at physical junctions]*. International Journal for Hybrid Microelectronics, 1984. **7**(3): p. 44-50.
71. Yovanovich, M.M. and V.W. Antonetti, *Application of thermal contact resistance theory to electronic packages*. Advances in Thermal Modeling of Electronic Components and Systems, 1988. **1**: p. 79-128.
72. Antonetti, V., T. Whittle, and R. Simons, *An approximate thermal contact conductance correlation*. Experimental/Numerical Heat Transfer in Combustion and Phase Change, ASME-HTD, 1991. **170**.
73. Franklin, T.A., *Ferrofluid flow phenomena*. 2003, Massachusetts Institute of Technology.
74. Matsch, L.W., *Electromagnetic and electromechanical machines*. 1977, New York: IEP.

